The Astrophysical Journal, 918:12 (20pp), 2021 September 1 https://doi.org/10.3847/1538-4357/ac0aed
© 2021. The American Astronomical Society. All rights reserved.

On the Origin of the Multi-GeV Photons from the Closest Burst with Intermediate Luminosity: GRB 190829A

N. Fraija[1], P. Veres[2], P. Beniamini[3], A. Galvan-Gamez[1], B. D. Metzger[4,5], R. Barniol Duran[6], and R. L. Becerra[1]
[1] Instituto de Astronomía, Universidad Nacional Autónoma de México, Apdo. Postal 70-264, Cd. Universitaria, Ciudad de México 04510, Mexico; nifraija@astro.unam.mx
[2] Center for Space Plasma and Aeronomic Research (CSPAR), University of Alabama in Huntsville, Huntsville, AL 35899, USA
[3] TAPIR, Mailcode 350-17, California Institute of Technology, Pasadena, CA 91125, USA
[4] Columbia Astrophysics Laboratory, Columbia University, New York, NY 10027, USA
[5] Center for Computational Astrophysics, Flatiron Institute, New York, NY 10010, USA
[6] Department of Physics and Astronomy, California State University, Sacramento, 6000 J Street, Sacramento, CA 95819-6041, USA
Received 2020 March 29; revised 2021 April 25; accepted 2021 June 12; published 2021 August 30

Abstract

Very high energy (VHE) emission is usually interpreted in the synchrotron self-Compton scenario and expected from the low-redshift and high-luminosity gamma-ray bursts (GRBs), such as GRB 180720B and GRB 190114C. Recently, the H.E.S.S. telescopes reported VHE emission from one of the closest bursts, GRB 190829A, which was associated with the supernova 2019oyw. In this paper, we present a temporal and spectral analysis from optical bands to the Fermi-LAT energy range over multiple observational periods beginning after the trigger time and extending for almost 3 months. We show that the X-ray and optical observations are consistent with synchrotron forward-shock emission evolving between the characteristic and cooling spectral breaks during the early and late afterglow in a uniform-density medium. Modeling the light curves together with the spectral energy distribution, we show that the outflow expanded with an initial bulk Lorentz factor of $\Gamma \sim 30$, which is high for low-luminosity GRBs and low for high-luminosity GRBs. The values of the initial bulk Lorentz factor and the isotropic-equivalent energy suggest that GRB 190829A is an intermediate-luminosity burst; consequently, it becomes the first burst of this class to be detected in the VHE gamma-ray band by an imaging atmospheric Cherenkov telescope and, in turn, the first event to not be simultaneously observed by the Fermi-LAT instrument. Analyzing the intermediate-luminosity bursts with $z \lesssim 0.2$, such as GRB 130702A, we show that bursts with intermediate luminosities are potential candidates to be detected in VHEs.

Unified Astronomy Thesaurus concepts: High energy astrophysics (739)

1. Introduction

Observational evidence has firmly established that gamma-ray bursts (GRBs) lasting longer than a few seconds are associated with the core collapse (CC) of massive stars (Woosley 1993) leading to supernovae (SNe; Galama et al. 1998; Bloom et al. 1999; Woosley & Bloom 2006). Based on the isotropic-equivalent luminosity in the gamma-ray band and the opening angle, some authors have classified GRBs as low-luminosity (ll) GRBs with $L_{\rm iso} \lesssim 10^{48.5}$ erg s^{-1}, intermediate-luminosity (il) GRBs with $10^{48.5}$ erg s^{-1} $\lesssim L_{\rm iso} \lesssim 10^{49.5}$ erg s^{-1}, and high-luminosity (hl) GRBs with $L_{\rm iso} \gtrsim 10^{49.5}$ erg s^{-1} (Bromberg et al. 2011; Hjorth 2013; Cano et al. 2017). Whereas llGRBs are connected with the shock breakouts[7] and hlGRBs are associated with emerging collimated jets (Bromberg et al. 2011), there is no clear association for ilGRBs (Schulze et al. 2014). To date, there are six confirmed GRB SNe detected within $z \lesssim 0.2$: GRB 980425/SN 1998bw (Galama et al. 1998), GRB 060218/SN 2006aj (Campana et al. 2006), GRB 100316D/SN 2010bh (Cano et al. 2011), and GRB 171205A/SN 2017iuk (Izzo et al. 2019), classified as llGRBs; GRB 130702A/SN 2013dx (D'Elia et al. 2015), classified as an ilGRB; and GRB 030329/SN 2003dh (Hjorth et al. 2003), classified as an hlGRB.[8]

Low-redshift and hlGRBs are potential candidates to produce very high energy (VHE $\geqslant 10$ GeV) photons during the prompt emission and afterglow (e.g., Ajello et al. 2019; Fraija et al. 2019a; Wang et al. 2019). During the afterglow phase, electrons are shock-accelerated and cooled down by the synchrotron process that radiates photons from radio to gamma rays. The maximum photon energy radiated by the synchrotron process during the deceleration phase becomes $\sim$5–10 GeV $\left(\frac{\Gamma(t)}{100}\right)(1+z)^{-1}$, where $\Gamma(t)$ is the bulk Lorentz factor (decaying with time), and z is the redshift (Abdo et al. 2009; Piran & Nakar 2010; Barniol Duran & Kumar 2011). Another cooling process is the synchrotron self-Compton (SSC) process; synchrotron photons are scattered above tens of GeV by the same electron population (Zhang & Mészáros 2001; Fraija 2015; Fraija et al. 2017a, 2019a). Recently, VHE photons with energies above 100 GeV were detected by the Major Atmospheric Gamma Imaging Cherenkov (MAGIC; Acciari et al. 2019) and the High Energy Stereoscopic System (H.E.S.S.; Abdalla et al. 2019) telescopes from high-luminosity bursts GRB 180720B and GRB 190114C, respectively. The high-energy and VHE photons detected by the Fermi Large Area Telescope (LAT), H.E.S.S., and MAGIC beyond the synchrotron limit were interpreted in the SSC forward-shock

[7] If llGRBs are shock breakouts, we should distinguish between the injected luminosity and the observed one, since they will be very different.

[8] Due to the luminosity and opening angle, GRB 161219B/SN 2016jca cannot be classified as an llGRB or ilGRB (Cano et al. 2017; Ashall et al. 2019).

(FS) scenario (Fraija et al. 2019c, 2019a; Zhang 2019). On the other hand, llGRBs, characterized by being less energetic and having opening angles $\gtrsim 30°$, are not natural candidates to emit VHE photons. So far, no llGRB has been associated with a high-energy or VHE photon. An interesting case study in this aspect is ilGRBs, which have luminosities between llGRBs and hlGRBs (D'Elia et al. 2015; Cano et al. 2017).

The Burst Alert Telescope (BAT) on board the Swift satellite triggered on GRB 190829A on 2019 August 29 at 19:56:44.60 UT (Dichiara et al. 2019). The H.E.S.S. telescopes followed up the afterglow of GRB 190829A. A preliminary on-site analysis of these observations showed a $>5\sigma$ gamma-ray excess in coincidence with the direction of GRB 190829A (de Naurois & H.E.S.S. Collaboration 2019). This burst, associated with a Type Ic-BL SN (de Ugarte Postigo et al. 2019), was followed up by a large-scale campaign with several instruments on board satellites and ground telescopes that covered most of the electromagnetic spectrum. Recently, Chand et al. (2020) discussed the VHE emission detected from GRB 190829A in terms of the shock breakout scenario.

Classified as an intermediate-luminosity burst and associated with the broad-line Type Ic SN 2013dx (D'Elia et al. 2015), GRB 130702A was detected at different wavelengths ranging from radio to high-energy gamma rays. The Gamma-ray Burst Monitor (GBM) on board the Fermi satellite triggered on GRB 130702A on 2013 July 2 at 00:05:23.079 UTC. The Fermi-LAT instrument detected photons from this burst above >100 MeV within 2200 s (Toy et al. 2016).

In this paper, we present a detailed data analysis of the multiwavelength observations of GRB 190829A. Using the best-fit parameters found after modeling the X-ray and optical light curves of this burst, we analyze the VHE emission reported by the H.E.S.S. experiment. Our model is generalized to study the mechanism involved to interpret the high-energy photons around other ilGRBs (e.g., GRB 130207A). We arrange the paper as follows. In Section 2, we show the multiwavelength observations and data reduction of GRB 190829A. In Section 3, we model and interpret the multi-wavelength observations. We discuss our results around GRB 190829A in Section 4. In Section 5, we present the analysis and discussion of the multi-GeV photons reported in GRB 190829A and GRB 130702A, and finally, in Section 6, we summarize. We adopt the convention $Q_{\rm x} = Q/10^{\rm x}$ in cgs units throughout this paper.

2. GRB 190829A

2.1. Observations and Data Reduction

2.1.1. Fermi: GBM Observations

The Fermi GBM instrument triggered and localized GRB 190829A on 2019 August 29 at 19:55:53.13 UT. We retrieve GBM data from the public database at the Fermi website.[9] Flux values are derived using the spectral analysis package Rmfit version 4.3.2.[10] We use the time-tagged event files of the Na I detectors (5, 6, 7, and 9) and the BGO detector B1. Table 1 corresponds to the values of the spectral analysis of GRB 190829A using GBM data during the time interval [–2.0; 68.0] s. During this interval, we observe an initial pulse followed by a brighter peak: the initial pulse between [−2.0; 12.0] s and the brighter peak between [46.0; 68.0] s, which correspond to total isotropic energies of $E_{\gamma,\rm iso} = (9.151 \pm 0.504) \times 10^{49}$ and $(2.967 \pm 0.032) \times 10^{50}$ erg, respectively, and peak energies of (67.88 ± 23.3) and (11.47 ± 0.360) keV, respectively. We calculate these values considering the energy range of 1 keV–10 MeV. This table shows the time interval (column 1), the low- (column 2) and high-energy (column 3) spectral indexes of the Band function, the peak energy (column 4), the isotropic-equivalent energy (column 5), and the observed flux (column 6). Although we consider the power law (PL) with exponential cutoff, the blackbody (BB; Planck function), and the Band function (Band et al. 1993), the time-resolved spectra best fit the Band function. To assess the quality of a spectral fit, we use the traditional χ^2 statistics.

2.1.2. Fermi: LAT Observations

The Fermi-LAT instrument performed a search for high-energy emission in different time windows around the position of this burst, and upper limits with a 95% confidence level in the 0.1–1 GeV energy range were derived (Piron et al. 2019). Considering a PL function $\propto \epsilon_\gamma^{-\Gamma_{\rm LAT}}$ with a photon index of $\Gamma_{\rm LAT} = \beta_{\rm LAT} + 1 = 2.0$, the LAT upper limits were 5.3×10^{-10}, 3.2×10^{-10}, 1.4×10^{-10}, and 1.8×10^{-10} erg cm^{-2} s^{-1} for time windows of 0–1.1, 0–10, 10–30, and 15–30 ks, respectively.

2.1.3. Swift: UVOT Observations

Observations with the UltraViolet and Optical Telescope (UVOT; Roming et al. 2006) on board Swift started 106 s after the BAT trigger (Oates et al. 2019). This instrument detected an emission consistent with the afterglow in the V, B, white, and U bands. Analyzing the afterglow spectrum, Valeev et al. (2019) found absorption lines of Ca, H, and K doublets, identifying this burst with DSS galaxy J025810.28–085719.2 at a redshift of $z = 0.0785 \pm 0.005$. We retrieve UVOT data from the publicly available database at the official Swift website.[11] We calculate the observed fluxes and their corresponding uncertainties using the standard conversion for the AB magnitude system shown in Fukugita et al. (1996). The optical data are corrected by the galactic extinction using the relation derived in Becerra et al. (2019). We use the value of $\beta_{\rm O} = 0.48$ for optical filters and a reddening of $E_{B-V} = 0.05$ (Dichiara et al. 2019).

2.1.4. Swift: BAT and XRT Observations

The Swift-BAT instrument triggered on GRB 190829A on 2019 August 29 at 19:56:44.60 UT (Dichiara et al. 2019). The instrument located this burst with coordinates R.A.(J2000) $= 02^{\rm h}58^{\rm m}10^{\rm s}$ and decl. $= -08^{\rm d}58'03''$ with an uncertainty of $3'$. The Swift XRT instrument started detecting GRB 190829A at 19:58:21.9 UT, 97.3 s after the BAT trigger. This instrument monitored GRB 190829A in the windowed-timing (WT) mode with a spectrum exposure of 128 s and the photon-counting (PC) mode with a spectrum exposure of 10.8 ks. We retrieve Swift data from the publicly available database at the official Swift website.[12] The flux density at 10 keV is transformed to 1 keV using the conversion factor derived in Evans et al. (2010).

[9] http://fermi.gsfc.nasa.gov/ssc/data
[10] https://fermi.gsfc.nasa.gov/ssc/data/analysis/rmfit/
[11] https://www.swift.ac.uk/archive/obs.php
[12] https://www.swift.ac.uk/burst_analyser/00922968/

Table 1
Spectral Analysis Using the GBM Data

Time Interval (s) (1)	$\alpha_{\rm Band}$ (2)	$\beta_{\rm Band}$ (3)	$E_{\rm peak}$ (keV) (4)	$E_{\rm iso}$ (erg) (5)	F (erg cm^{-2} s^{-1}) (6)
Initial pulse[a]					
[−2.0; 0.0]	-0.10 ± 0.00	-1.32 ± 0.10	11.4 ± 1.7	$(3.0 \pm 0.2) \times 10^{49}$	$(2.22 \pm 0.31) \times 10^{-7}$
[0.0; 2.0]	-0.72 ± 0.00	-1.80 ± 0.08	62.3 ± 25.1	$(3.7 \pm 0.2) \times 10^{49}$	$(6.41 \pm 0.39) \times 10^{-7}$
[2.0; 4.0]	-1.15 ± 0.00	-2.53 ± 0.41	59.0 ± 12.4	$(1.1 \pm 0.1) \times 10^{49}$	$(3.05 \pm 0.34) \times 10^{-7}$
[4.0; 6.0]	-0.10 ± 0.00	-2.15 ± 0.13	20.5 ± 4.3	$(7.3 \pm 0.4) \times 10^{48}$	$(1.79 \pm 0.24) \times 10^{-7}$
[6.0; 8.0]	-0.10 ± 0.00	-2.50 ± 0.38	15.1 ± 3.9	$(2.9 \pm 0.2) \times 10^{48}$	$(7.30 \pm 0.81) \times 10^{-8}$
[8.0; 10.0]	-0.10 ± 0.00	-2.38 ± 0.32	11.4 ± 1.7	$(2.0 \pm 0.1) \times 10^{48}$	$(4.69 \pm 0.16) \times 10^{-8}$
[10.0; 12.0]	-0.10 ± 0.00	-2.50 ± 0.38	15.2 ± 10.4	$(1.0 \pm 0.1) \times 10^{48}$	$(2.61 \pm 0.77) \times 10^{-8}$
Brighter peak[b]					
[46.0; 48.0]	-1.11 ± 0.17	-2.20 ± 0.18	14.0 ± 9.9	$(5.1 \pm 0.1) \times 10^{48}$	$(1.09 \pm 0.21) \times 10^{-7}$
[48.0; 50.0]	-1.18 ± 0.93	-2.46 ± 0.03	12.0 ± 2.3	$(4.7 \pm 0.1) \times 10^{49}$	$(9.47 \pm 0.03) \times 10^{-7}$
[50.0; 52.0]	-1.11 ± 1.12	-2.48 ± 0.02	10.8 ± 2.6	$(7.4 \pm 0.1) \times 10^{49}$	$(1.47 \pm 0.03) \times 10^{-6}$
[52.0; 54.0]	-0.82 ± 1.46	-2.50 ± 0.02	11.1 ± 2.0	$(6.5 \pm 0.1) \times 10^{49}$	$(1.34 \pm 0.02) \times 10^{-6}$
[54.0; 56.0]	-1.19 ± 1.22	-2.58 ± 0.04	10.0 ± 3.9	$(4.6 \pm 0.1) \times 10^{49}$	$(8.44 \pm 0.21) \times 10^{-7}$
[56.0; 58.0]	-1.11 ± 0.17	-2.58 ± 0.05	8.9 ± 1.3	$(2.82 \pm 0.03) \times 10^{49}$	$(4.92 \pm 0.17) \times 10^{-7}$
[58.0; 60.0]	-1.11 ± 0.17	-2.64 ± 0.09	9.7 ± 1.6	$(1.43 \pm 0.02) \times 10^{49}$	$(2.54 \pm 0.15) \times 10^{-7}$
[60.0; 62.0]	-1.11 ± 0.17	-2.66 ± 0.13	7.1 ± 4.2	$(8.4 \pm 0.1) \times 10^{48}$	$(1.27 \pm 0.13) \times 10^{-7}$
[62.0; 64.0]	-1.11 ± 0.17	-2.50 ± 0.17	11.5 ± 1.7	$(5.2 \pm 0.1) \times 10^{48}$	$(1.05 \pm 0.16) \times 10^{-7}$
[64.0; 66.0]	-1.11 ± 0.17	-2.29 ± 0.29	11.5 ± 1.7	$(2.52 \pm 0.03) \times 10^{48}$	$(5.20 \pm 1.78) \times 10^{-8}$
[66.0; 68.0]	-1.11 ± 0.17	-2.55 ± 0.38	20.6 ± 10.8	$(1.81 \pm 0.02) \times 10^{48}$	$(4.33 \pm 0.94) \times 10^{-8}$

Notes.
[a] The total isotropic-equivalent energy and the peak energy correspond to $(9.151 \pm 0.504) \times 10^{49}$ erg and 67.88 ± 23.34 keV, respectively.
[b] The total isotropic-equivalent energy and the peak energy correspond to $(2.967 \pm 0.032) \times 10^{50}$ erg and 11.47 ± 0.36 keV, respectively.

2.1.5. H.E.S.S.: VHE Gamma-Ray Observations

The H.E.S.S. telescopes reported the detection of VHE gamma-ray emission with a significance of 5σ, compatible with the direction of GRB 190829A (de Naurois & H.E.S.S. Collaboration 2019). Observations started on 2019 July 30 at 00:16 UTC and lasted 3.9 hr.

2.1.6. GRB/SN Observations

GROND, mounted at the 2.2 m MPG telescope at the ESO La Silla Observatory, found a relatively sharp growth in all bands between 4.5 and 5.5 days after the trigger time (Bolmer et al. 2019). Terreran et al. (2019) studied the spectrum of the optical afterglow with the Low-Resolution Imaging Spectrometer. They found identical features consistent with a broad-line SN and the X-ray analysis reported by Osborne et al. (2019). Besides, de Ugarte Postigo et al. (2019) found evidence of broad absorption lines with expansion velocities similar to SN 1998bw. It confirmed the association of SN 2019oyw (classified as a Type Ic-BL)[13] with GRB 190829A.

2.2. Analysis of the Multiwavelength Observations

2.2.1. GBM Data Analysis

The upper panel in Figure 1 shows the gamma-ray light curve and the evolution of the peak ($E_{\rm peak}$), low- ($\alpha_{\rm Band}$), and high-energy ($\beta_{\rm Band}$) spectral indexes of GRB 190829A. The initial gamma-ray pulse is shown by open circles and the brighter peak by filled circles. These subpanels are ordered from top to bottom: the low-energy spectral index, high-energy spectral index, energy peak, and gamma-ray light curve obtained in the 10–1000 keV energy range. To fit the entire gamma-ray light curve, we use the functions given by $F_\nu(t) \propto e^{-\frac{\tau_1}{t-t_0}} F_{\rm k}$, with $F_{\rm k} = e^{-\frac{t-t_0}{\tau_2}}$ (Norris et al. 2005) for the initial pulse and $F_{\rm k} = \left(\frac{t-t_0}{t_0}\right)^{-\alpha_\gamma}$ (Vestrand et al. 2006) for the brighter peak. The term t_0 is the time of onset of the energy release, $\tau_{1(2)}$ is the timescale of the flux rise (decay), and α_γ is the PL decay index. To fit the evolution of the parameters ($E_{\rm peak}$, $\alpha_{\rm Band}$, and $\beta_{\rm Band}$), we use PL functions $\propto t^{-\delta}$ with δ a PL index. The linear least-squares (Lai et al. 1978) fitting implemented in the ROOT scientific software (Brun & Rademakers 1997) is used to find the best-fit values, which are reported in Table 2. To find the minimum variability timescale for this burst, we use the method proposed by Bhat et al. (2012). This variability timescale corresponds to 214.7 ± 6.9 ms.

2.2.1.1. Evolution of the Spectral Parameters

During the first pulse, the lower-energy photon index is not well constrained in the time-resolved analysis. The peak energy is low, and the low-energy part of the Band spectrum mostly falls outside the GBM range.

During the brighter gamma-ray peak, the Band-function parameters are typical and similar to most bursts ($\alpha_{\rm Band} \approx -1.1$ and $\beta_{\rm Band} \approx -2.5$). The value of the low-energy spectral index of ≈ -1.1 can be explained within the synchrotron model in a decay magnetic field (Uhm & Zhang 2014), magnetic reconnection/dissipation models (Beniamini & Piran 2014; Beniamini et al. 2017, 2018; Lazarian et al. 2019), and dissipative photosphere models (Pe'er et al. 2006; Lazzati & Begelman 2010; Ahlgren et al. 2015; Vurm & Beloborodov 2016). It is also possible to have a combination of the synchrotron and photospheric models that evolve differently with time (e.g., Beniamini & Giannios 2017).

[13] http://www.rochesterastronomy.org/snimages/

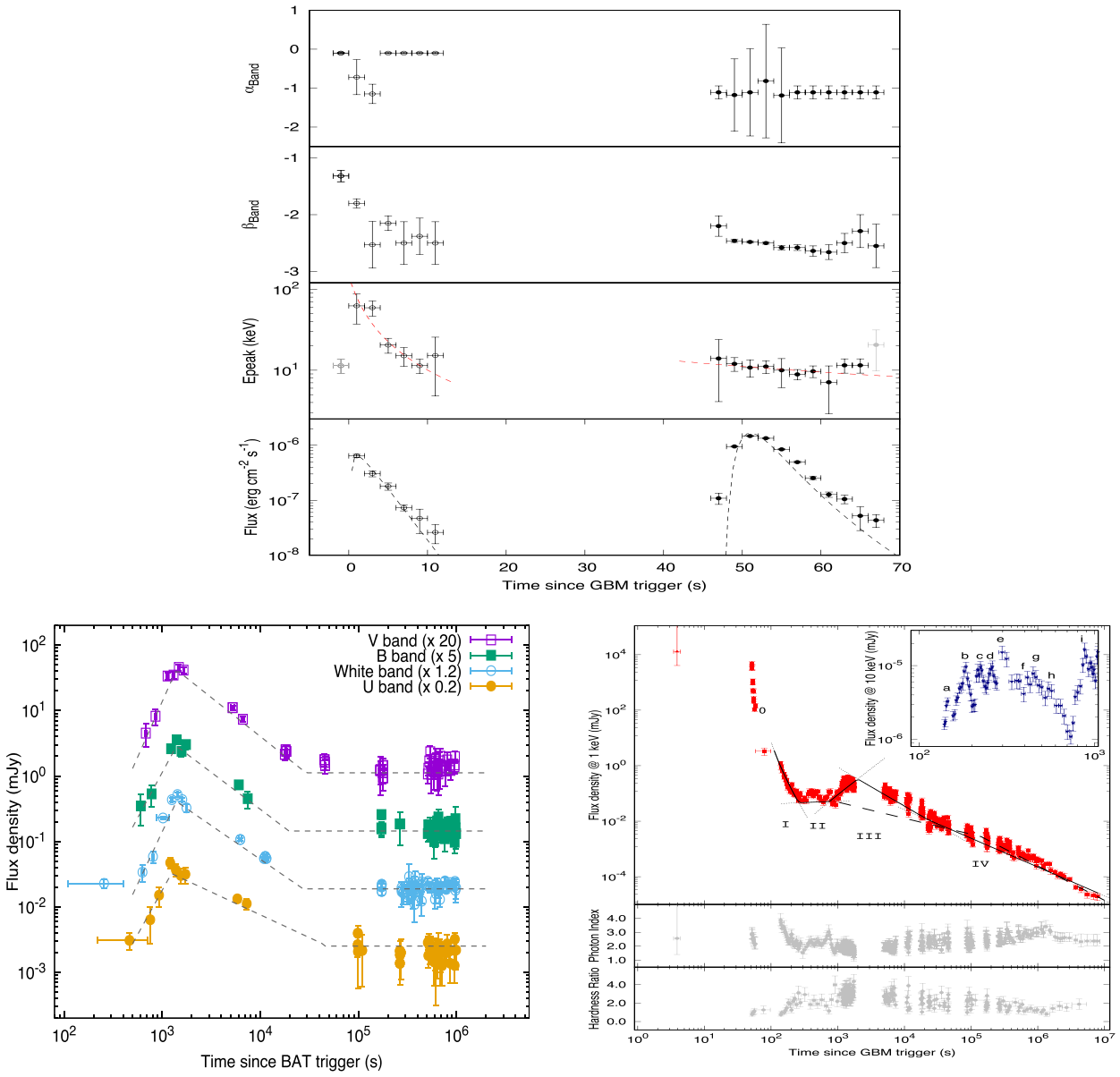

Figure 1. The upper panel shows the gamma-ray light curve and the evolution of the peak, low-, and high-energy spectral indexes of GRB 190829A. From top to bottom: low-energy spectral index, high-energy spectral index, energy peak, and gamma-ray light curve obtained in the 10–1000 keV energy range. We show the initial gamma-ray pulse with open circles and the brighter peak with filled circles. Lines in all panels correspond to the best-fit functions. The lower left panel shows the Swift UVOT light curve in the *V*, *B*, white, and *U* bands. The dashed gray curves in all color filters represent the best-fit BPL functions. The lower right panel shows the X-ray light curve at 1 keV and the small box at 10 keV. At 1 keV, five phases are labeled: "0" is the initial PL segment, "I" is the steep decay, "II" is the plateau phase, "III" is the X-ray flare, and "IV" is the canonical normal decay; At 10 keV, nine small peaks are labeled: "a," "b," "c," "d," "e," "f," "g," "h," and "i." We draw the best-fit curves in each phase. The middle subpanel corresponds to the photon index light curves, and the bottom subpanel corresponds to the hardness ratio light curve. The solid black lines correspond to the best-fit curves found in this work, and the dashed gray lines represent the best-fit curves reported by the Swift team.

2.2.2. UVOT Data Analysis

The lower left panel in Figure 1 shows the UV/optical light curves of GRB 190829A with the best-fit curves using broken power-law (BPL) functions. The light curves of the Swift UVOT obtained in the *V*, *B*, white, and *U* bands display that before $\approx$700 s, all color filters remain constant. Then, they increase as $F_\nu \propto t^{-\alpha_O}$, with $\alpha_O \approx -3$, reaching the maximum values at $\approx 1.4 \times 10^3$ s. Finally, they decrease with slopes of $\alpha_O \approx 1$ up to $\sim 3 \times 10^4$ s. After this time, the host galaxy dominates over the flux densities in all color filters. We obtain the best-fit parameters of each color filter using PL functions and the timescales of $\Delta t/t$. We calculate the timescales of $\Delta t/t$, adopting the peak time and Gaussian width as t and Δt, respectively (Chincarini et al. 2007). We report the best-fit values in Table 3.

2.2.3. BAT and XRT Data Analysis

The lower right panel in Figure 1 shows the X-ray light curves at 1 and 10 keV (top), the spectral evolution of the photon index (medium), and the hardness ratio (bottom). Five epochs, labeled "0," "I," "II," "III," and "IV" corresponding to the time intervals [52; 62], [82; 215], [215; 700], [700; 1.4×10^5], and $>1.4 \times 10^5$ s, respectively, are identified. We distinguish a precursor in this panel $\sim$3 s after the GBM

Table 2
The Best-fit Parameters from the Initial Pulse and the Brighter Peak Displayed in the GBM Light Curve

Event	Period (s)	τ_1 (s)	τ_2 (s)	α_γ	t_0 (s)	χ^2/ndf
Initial pulse	[−2.0; 10]	2.31 ± 0.06	0.39 ± 0.10	⋯	0.11 ± 0.06	0.81
Brighter peak	[46; 68]	32.2 ± 7.2	⋯	6.59 ± 1.65	43.6 ± 9.1	0.84

trigger time. The dashed gray lines represent the best-fit curves reported by the Swift team.[14] We fit all of the epochs with PL functions $\propto t^{-\alpha}$. Epoch 0 corresponds to the prompt emission fitted with a temporal index of $\alpha_{\rm X,I} = 2.72 \pm 0.28$. The steep decay in epoch I is fitted with a temporal index of $\alpha_{\rm X,I} = 3.53 \pm 0.70$, and the subsequent very shallow decay identified in epoch II is described with the temporal index of $\alpha_{\rm X,II} = 0.06 \pm 0.03$. In epoch III, the X-ray flare is modeled with a rising and falling slope of $\alpha_{\rm X,III,rise} = -(3.12 \pm 0.94)$ and $\alpha_{\rm X,III,dec} = (1.03 \pm 0.12)$, respectively, corresponding to a timescale of $\Delta t/t = 0.75 \pm 0.24$. Finally, the canonical normal decay in epoch IV is described using the values reported by the Swift analysis, a temporal index of $\alpha_{\rm X,IV} = 1.23 \pm 0.04$ after the temporal break of $t_{\rm br} = 1.4^{+0.17}_{-0.15} \times 10^5$ s. We report the best-fit values of the X-ray data in Table 4.

During epochs I and II (see the small box tucked within this panel), the X-ray light curve at 10 keV displays several peaks labeled "a," "b," "c," "d," "e," "f," "g," "h," and "i." We report the best-fit values of the rising and falling slopes with their corresponding timescales in Table 5.

Figure 2 shows the spectral energy distribution (SED) of GRB 190829A built with the optical and X-ray data at two different times (epoch III): 6.0×10^3 (left) and 1.8×10^4 (right) s. These SEDs are modeled with simple PLs with spectral indexes of $\beta_{\rm X} = 0.48 \pm 0.05$ and 0.47 ± 0.05, respectively. The gray dashed lines correspond to the best-fit curves obtained from XSPEC for a column density of $(7.9 \pm 0.6) \times 10^{21}$ cm^{-2}.

On the other hand, we analyze XRT data in the PC and WT mode with a PL and a BB model incorporated in XSPEC v.12.10.1 (Arnaud 1996) in 13 time windows between 100 and 1700 s, as shown in Table 6. This table shows the best-fit values using the PL and PL-plus-BB models. One can see that although in some time windows, the traditional χ^2 statistics are slightly better when we introduce a BB model, there is no clear evidence of a thermal component.

2.2.3.1. The Photon Index and Hardness Ratio Light Curves

The lower right panel in Figure 1 shows the spectral index ($\Gamma_{\rm ph}$; middle) and hardness ratio ($H_{\rm R}$; bottom) light curves. The hardness ratios associated with BAT and XRT data are defined by the photon fluxes in the ranges of (25–50 keV)/(15–25 keV) and (1.5–10 keV)/(0.3–1.5 keV), respectively (Evans et al. 2010). We analyze the evolution of the photon index and hardness ratio in each epoch.

Epoch 0. During the prompt emission, one can note that the photon index and hardness ratio exhibit a small degree of evolution. The photon index increases progressively from $\Gamma_{\rm ph,0} = 0.18$ to 0.28, and the hardness ratio decreases from $H_{\rm R,0} = 2.89$ to 2.17. The Pearson's correlation coefficient between the X-ray flux and the photon index is $r_{\rm F,\Gamma_{ph}} = 0.95$ with a p-value of 2×10^{-6}. It indicates that both variables are strongly correlated.

Epoch I. During the steep decay, the photon index and hardness ratio light curves exhibit the strongest evolution. These parameters vary significantly from $\Gamma_{\rm ph,I} = 4.15$ to 1.24 and from $H_{\rm R,I} = 0.59$ to 4.66, respectively. The maximum and minimum photon index corresponds to the maximum and minimum values of the light curve. Similarly, the maximum and minimum hardness ratio corresponds to the maximum and one of the minimum values of the light curve. Using the ROOT software package (Brun & Rademakers 1997), we successfully fit the photon index and hardness ratio as $\Gamma_{\rm ph,I} \propto t^{-0.75\pm0.06}$ (χ^2/ndf = 0.96) and $H_{\rm R,I} \propto t^{1.36\pm0.19}$ (0.95), respectively. The Pearson's correlation coefficient between the flux and the photon index is $r_{\rm F,\Gamma_{ph}} = 0.77$ with a p-value of 3×10^{-7}. It indicates a strong correlation between both variables.

Epoch II. During this epoch, the photon index and hardness ratio evolve rapidly among two maximum and minimum values. First, the photon index and hardness ratio vary from $\Gamma_{\rm ph,II} = 1.34$ to 2.32 and $H_{\rm R,II} = 3.05$ to 1.79, respectively. Next, once the X-ray flux decreases, the photon index and hardness ratio increase. Finally, these parameters evolve from $\Gamma_{\rm ph,II} = 2.61$ to 1.31 and $H_{\rm R,II} = 4.34$ to 1.45, respectively.

Epoch III. During the X-ray flare, the photon index and hardness ratio display random fluctuations around ≈3 and ≈2.5, respectively.

Epoch IV. During the canonical normal decay, we observe a very moderate spectral softening.

3. Interpretation and Modeling of the Multiwavelength Observations

3.1. Spin-down Millisecond Magnetar Model

The energy reservoir of a millisecond magnetar is the total rotation energy, which is given by

$$E = \frac{1}{2} I\, \Omega^2 \approx 2.6 \times 10^{52}\ {\rm erg}\ M_{\rm ns,1.4}^{\frac{3}{2}}\, P_{-3}^{-2}, \quad (1)$$

where P is the spin period associated with an angular frequency $\Omega = 2\pi/P$, and $I \simeq 1.3 \times 10^{45}\, M_{\rm ns,1.4}^{\frac{3}{2}}$ g cm^2 (Lattimer & Schutz 2005) is the neutron star (NS) moment of inertia, with $M_{\rm ns} = 1.4\, M_\odot M_{\rm ns,1.4}$ the NS mass.

The CC SN usually leaves a fraction of the stellar progenitor bound to the NS following the SN explosion. This fraction of material will begin to rotate into an accretion disk and fall back over a long period (Chevalier 1989; Woosley & Heger 2012; Quataert & Kasen 2012). For simplicity, we consider a fallback accretion rate given by (Metzger et al. 2018)

$$\dot{M} \simeq \frac{2}{3}\frac{M_{\rm fb}}{t_{\rm fb}} \begin{cases} 1 & t \ll t_{\rm fb}, \\ \left(\frac{t}{t_{\rm fb}}\right)^{-\frac{5}{3}} & t_{\rm fb} \ll t, \end{cases} \quad (2)$$

where $M_{\rm fb}$ is the accreting mass over a characteristic fallback time $t_{\rm fb}$. The dynamics of the magnetar with fallback accretion depends on the Alfvén ($r_{\rm m}$), corotation ($r_{\rm c}$), and light cylinder

[14] https://www.swift.ac.uk/xrt_live_cat/00922968/

Table 3
The Best-fit Parameters Obtained from the UVOT Light Curves

Band	Rise Index/Theory $-(\alpha_{O,r})$	Peak Time t_{br} ($\times 10^3$ s)	Decay Index/Theory ($\alpha_{O,\,d}$)	$\Delta t/t$	F_{cont} ($\times 10^{-2}$ mJy)	χ^2/ndf
V	$3.28 \pm 0.43/3.0$	1.39 ± 0.30	$1.19 \pm 0.30/0.86 \pm 0.13$	1.01 ± 0.22	5.58 ± 0.45	0.87
B	$2.87 \pm 0.41/3.0$	1.41 ± 0.32	$1.13 \pm 0.38/0.86 \pm 0.13$	0.68 ± 0.21	2.56 ± 0.34	1.25
White	$3.08 \pm 0.31/3.0$	1.38 ± 0.29	$1.03 \pm 0.25/0.86 \pm 0.13$	0.71 ± 0.23	1.31 ± 0.25	1.71
U	$2.80 \pm 0.32/3.0$	1.25 ± 0.39	$0.76 \pm 0.22/0.86 \pm 0.13$	0.73 ± 0.23	0.93 ± 0.09	0.81

Note. The theoretical values are estimated for $p = 2.15 \pm 0.17$.

(r_{lc}) radii, which are

$$r_m \simeq 2.2 \times 10^6\,\mathrm{cm}\, M_{ns,1.4}^{-\frac{1}{7}}\, \dot{M}_{-2}^{-\frac{2}{7}}\, B_{15}^{\frac{4}{7}}\, R_{ns,6.1}^{\frac{12}{7}},$$
$$r_c \simeq 1.7 \times 10^6\,\mathrm{cm}\, M_{ns,1.4}^{\frac{1}{3}}\, P_{-3}^{\frac{2}{3}},$$
$$r_{lc} \simeq 4.8 \times 10^6\,\mathrm{cm}\, P_{-3}, \quad (3)$$

respectively, and the spin evolution is given by the differential equation (Piro & Ott 2011)

$$I\frac{d\Omega}{dt} = -N_{dip} + N_{acc}, \quad (4)$$

where $R_{ns} \simeq 1.2 \times 10^6\,\mathrm{cm}\, R_{ns,6.1}$ is the NS radius and B is the strength of the dipole magnetic field. The terms N_{dip} and N_{acc} are the spin-down torques from the dipole emission and accretion, respectively. For $r_m \gtrsim R_{ns}$, these torques are (Parfrey et al. 2016)

$$N_{dip} \simeq \begin{cases} \dfrac{\mu^2\Omega^3}{c^3}\dfrac{r_{lc}^2}{r_m^2} & r_m \lesssim r_{lc}, \\ \dfrac{\mu^2\Omega^3}{c^3} & r_{lc} \lesssim r_m, \end{cases} \quad (5)$$

and

$$N_{acc} = \dot{M}(G\, M_{ns}\, r_m)^{\frac{1}{2}}\left[1 - \left(\frac{r_m}{r_c}\right)^{\frac{3}{2}}\right], \quad (6)$$

where $\mu = BR_{ns}^3$ is the magnetic moment and G is the gravitational constant.

The magnetar will accrete material depending on the location of the Alfvén radius relative to the corotation radius. For $r_m \lesssim r_c$, the magnetar will accrete; otherwise, the system could enter into the propeller regime (e.g., see Campana et al. 1998). We can calculate the spin period that delineates both regimes and also happens to be the steady-state evolution of the system using the condition $r_m = r_c$. In this case, the spin period in equilibrium becomes

$$P_{eq} \simeq 1.5 \times 10^{-3}\,\mathrm{s}\, B_{15}^{\frac{6}{7}}\, R_{ns,6.1}^{\frac{18}{7}}\, M_{ns,1.4}^{-\frac{5}{7}}\, \dot{M}_{-2}^{-\frac{3}{7}}, \quad (7)$$

which is reached during the time interval given by $I\Omega_{eq}/\dot{M}(G\, M_{ns}\, r_m)^{\frac{1}{2}}$ with $\Omega_{eq} = 2\pi/P_{eq}$.

The electromagnetic spin-down luminosity can be estimated solving the differential equation, which is given by

$$L_{sd} = \Omega(N_{dip} - N_{acc}). \quad (8)$$

3.1.1. GRB Prompt Emission and the Magnetization Parameter

The prompt emission in the Poynting flux–dominated regime will be generated by magnetic reconnections, which could not induce internal shell collisions. In both cases, the magnetization parameter plays an important role. In some magnetic dissipation models, the magnetization parameter is expected to be similar to the bulk Lorentz factor and lies in the range of $100 \lesssim \sigma \lesssim 3000$ (Liang et al. 2010; Ghirlanda et al. 2012; Beniamini & Giannios 2017).

Irrespective of the model, the magnetization parameter is defined by

$$\sigma = \frac{L_j}{\dot{M}_j\, c^2}, \quad (9)$$

where $\dot{M}_j$ is the rate at which the baryon loading is ejected from the NS surface, and $L_j = L_{sd}$ (Bucciantini et al. 2009). In the case of a weakly magnetized wind, it can be written as

$$\dot{M}_j \simeq \dot{M}_\nu\, f_{cent} \begin{cases} \dfrac{R_{ns}}{2\, r_m} & r_m \lesssim r_{lc} \\ \dfrac{R_{ns}}{2\, r_{lc}} & r_{lc} \lesssim r_m, \end{cases} \quad (10)$$

with $\dot{M}_\nu = \dot{M}_{\nu,ob}(t) + \dot{M}_{\nu,acc}(t)$, $f_{cent} = e^{\left(\frac{P_c}{P}\right)^{\frac{3}{2}}}$, and $P_c \simeq 2.7\, R_{ns}^{\frac{1}{2}}\, r_m^{-\frac{1}{2}}\, M_{1.4}^{-\frac{1}{2}}$. The terms $\dot{M}_{\nu,ob}(t)$ and $\dot{M}_{acc}$ are associated with the mass-loss rate due to different sources of neutrinos. The term $\dot{M}_{\nu,ob}(t)$, defined by

$$\dot{M}_{\nu,ob}(t) = 3 \times 10^{-4}\left(1 + \frac{t}{t_{kh}}\right)^{-\frac{5}{2}} e^{-\frac{t}{t_{thin}}}\, M_\odot\, \mathrm{s}^{-1}, \quad (11)$$

is due to the neutrino ablation (Metzger et al. 2011), and the term $\dot{M}_{\nu,acc}(t)$, defined by

$$\dot{M}_{\nu,acc}(t) = 1.2 \times 10^{-5}\, M_{1.4}\, \dot{M}_{-2}^{\frac{5}{3}}\, M_\odot\, s^{-1}, \quad (12)$$

is due to the accretion (Piro & Ott 2011). The cooling timescale $t_{kh} \approx 2$ s corresponds to Kelvin–Helmholtz, and $t_{thin} \approx (10\text{–}30)$ s corresponds to the timescale when the NS becomes optically thin to neutrinos (Metzger et al. 2018).

3.2. Synchrotron Light Curves from External Shocks

3.2.1. Light Curves from FSs (No Injection)

It is widely accepted that the synchrotron FS model can explain the X-ray, optical, and radio observations in GRB afterglows. The shape of the synchrotron light curves depends on the density profile of the circumburst medium (i.e., uniform density or wind). The characteristic and cooling spectral breaks

Table 4
The Best-fit Parameter Obtained from Different Epochs Identified in the Swift (BAT + XRT) Light Curve

Epoch	Period	Index/Theory	Peak Time (s)	$\Delta t/t$	χ^2/ndf
0	52–62 s	$2.72 \pm 0.28/3.1 \pm 0.15$	⋯	⋯	0.75
I	82–215 s	$3.53 \pm 0.70/3.1 \pm 0.15$	⋯	⋯	0.81
II	215–700 s	$0.06 \pm 0.03/0$	⋯	⋯	0.84
III	$700 - 1.4^{+0.17}_{-0.15} \times 10^5$ s	$-(3.12 \pm 0.94)/-3.0$ $1.03 \pm 0.12/0.86 \pm 0.13$	1.4×10^3	0.75 ± 0.24	0.83
IV[a]	$\geqslant 1.4^{+0.17}_{-0.15} \times 10^5$ s	$1.23 \pm 0.04/1.11 \pm 0.13$	⋯	⋯	0.91

Note. The theoretical values are estimated for $p = 2.15 \pm 0.17$.
[a] These values are taken from the Swift analysis.

Table 5
The Best-fit Parameters of the Multipeaks Obtained from the XRT Light Curve at 10 keV

Peaks	Index (α_X)	Peak Time (s)	$\Delta t/t$	χ^2/ndf
a	$-(22.9 \pm 6.2)$ 3.5 ± 1.3	97.5	0.15	1.7
b	$-(11.0 \pm 0.9)$ 13.05 ± 1.5	133.0	0.14	1.1
c	$-(25.6 \pm 3.5)$ 6.8 ± 1.6	172.0	0.12	1.4
d	$-(16.3 \pm 3.4)$ 16.4 ± 5.9	208.0	0.14	0.1
e	$-(19.7 \pm 3.2)$ 9.1 ± 7.1	253.0	0.17	0.1
f	$-(11.7 \pm 9.1)$ 3.3 ± 2.1	364.0	0.12	0.2
g	$-(8.9 \pm 5.2)$ 5.3 ± 2.4	401.0	0.16	0.2
h	$-(7.9. \pm 6.5)$ 5.8 ± 2.7	508.0	0.22	0.6
i	$-(19.9 \pm 3.8)$ 10.2 ± 2.5	840.0	0.11	0.5

and the maximum flux of synchrotron emission evolving in a uniform-density (wind) medium are $\epsilon_m^{syn} \propto \Gamma^4(t^{-1}\Gamma^2)$, $\epsilon_c^{syn} \propto t^{-2}\,\Gamma^{-4}(t\,\Gamma^2)$, and $F_{max}^{syn} \propto t^3\Gamma^8(t^0\,\Gamma^2)$, respectively. We briefly introduce the predicted synchrotron light curves during the early and late afterglow for the thick- and thin-shell regimes.

3.2.1.1. The Early Afterglow

Before the jet decelerates, the bulk Lorentz factor is constant, $\Gamma \propto t^0$ (coasting phase). In this phase, the synchrotron spectral breaks and maximum flux in the uniform-density (wind) medium are $\epsilon_m^{syn} \propto t^0(t^{-1})$, $\epsilon_c^{syn} \propto t^{-2}(t)$, and $F_{max} \propto t^3(t^0)$, respectively. The predicted synchrotron light curves in the uniform-density (wind) medium for the fast- and slow-cooling regimes are (Sari & Piran 1999a, 1999b)

$$F_\nu^{syn} \propto \begin{cases} t^2(t^{\frac{1}{2}})\epsilon_\gamma^{-\frac{1}{2}}, & \epsilon_c^{syn} < \epsilon_\gamma < \epsilon_m^{syn}, \\ t^2(t^{\frac{2-p}{2}})\epsilon_\gamma^{-\frac{p}{2}}, & \epsilon_m^{syn} < \epsilon_\gamma, \end{cases} \quad (13)$$

and

$$F_\nu^{syn} \propto \begin{cases} t^3(t^{\frac{1-p}{2}})\epsilon_\gamma^{-\frac{p-1}{2}}, & \epsilon_m^{syn} < \epsilon_\gamma < \epsilon_c^{syn}, \\ t^2(t^{\frac{2-p}{2}})\epsilon_\gamma^{-\frac{p}{2}}, & \epsilon_c^{syn} < \epsilon_\gamma, \end{cases} \quad (14)$$

respectively, where p is the spectral index of the electrons' energy distribution.

3.2.1.2. The Thick-shell Regime

During this regime, the bulk Lorentz factor, the synchrotron spectral breaks, and the maximum flux in the uniform-density (wind) medium evolve as $\Gamma \propto t^{-\frac{1}{4}}(t^0)$, $\epsilon_m^{syn} \propto t^{-1}(t^{-1})$, $\epsilon_c^{syn} \propto t^{-1}(t)$, and $F_{max} \propto t(t^0)$, respectively. The predicted synchrotron light curves in the uniform-density (wind) medium for the fast- and slow-cooling regimes are (Gao et al. 2013; Yi et al. 2013)

$$F_\nu^{syn} \propto \begin{cases} t^{\frac{1}{2}}(t^{\frac{1}{2}})\epsilon_\gamma^{-\frac{1}{2}}, & \epsilon_c^{syn} < \epsilon_\gamma < \epsilon_m^{syn}, \\ t^{-\frac{p-2}{2}}(t^{-\frac{p-2}{2}})\epsilon_\gamma^{-\frac{p}{2}}, & \epsilon_m^{syn} < \epsilon_\gamma, \end{cases} \quad (15)$$

and

$$F_\nu^{syn} \propto \begin{cases} t^{-\frac{p-3}{2}}(t^{-\frac{p-1}{2}})\epsilon_\gamma^{-\frac{p-1}{2}}, & \epsilon_m^{syn} < \epsilon_\gamma < \epsilon_c^{syn}, \\ t^{-\frac{p-2}{2}}(t^{-\frac{p-2}{2}})\epsilon_\gamma^{-\frac{p}{2}}, & \epsilon_c^{syn} < \epsilon_\gamma, \end{cases} \quad (16)$$

respectively.

3.2.1.3. The Deceleration Phase (the Thin-shell Regime)

In the deceleration phase, the bulk Lorentz factor in the uniform-density (wind) medium evolves as $\Gamma \propto t^{-\frac{3}{8}}(t^{-\frac{1}{4}})$. The synchrotron spectral breaks and the maximum flux in the uniform-density (wind) medium become $\epsilon_m^{syn} \propto t^{-3/2}(t^{-3/2})$, $\epsilon_c^{syn} \propto t^{-\frac{1}{2}}(t^{\frac{1}{2}})$, and $F_{max} \propto t^0(t)$, respectively. The predicted synchrotron light curves in the uniform-density (wind) medium for the fast- and slow-cooling regimes are (Sari et al. 1998;

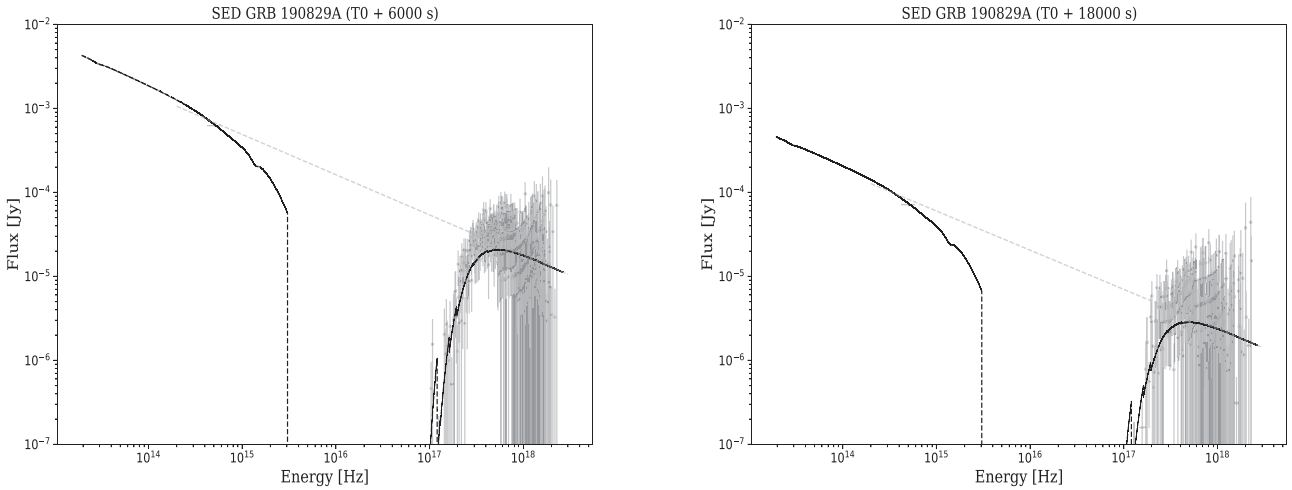

Figure 2. We show the broadband SEDs of the X-ray and optical observations at 6000 (left) and 18,000 (right) s. The dashed gray lines in each panel correspond to the best-fit curve from XSPEC.

Chevalier & Li 2000)

$$F_\nu^{\rm syn} \propto \begin{cases} t^{-\frac{1}{4}}\,(t^{-\frac{1}{4}})\,\epsilon_\gamma^{-\frac{1}{2}}, & \epsilon_{\rm c}^{\rm syn} < \epsilon_\gamma < \epsilon_{\rm m}^{\rm syn}, \\ t^{-\frac{3p-2}{4}}(t^{-\frac{3p-2}{4}})\,\epsilon_\gamma^{-\frac{p}{2}}, & \epsilon_{\rm m}^{\rm syn} < \epsilon_\gamma, \end{cases} \tag{17}$$

and

$$F_\nu^{\rm syn} \propto \begin{cases} t^{-\frac{3p-3}{4}}(t^{-\frac{3p-1}{4}})\,\epsilon_\gamma^{-\frac{p-1}{2}}, & \epsilon_{\rm m}^{\rm syn} < \epsilon_\gamma < \epsilon_{\rm c}^{\rm syn}, \\ t^{-\frac{3p-2}{4}}(t^{-\frac{3p-2}{4}})\,\epsilon_\gamma^{-\frac{p}{2}}, & \epsilon_{\rm c}^{\rm syn} < \epsilon_\gamma, \end{cases} \tag{18}$$

respectively.

3.2.2. Light Curves from FSs (Injection)

Continuous energy injection by the central engine on the GRB afterglow can produce refreshed shocks. A continuous luminosity of the central engine can be described by

$$L_{\rm inj}(t) = L_0\left(\frac{t}{t_{\rm fb}}\right)^{-{\rm q}}, \tag{19}$$

where q is the energy injection index and $L_{\rm inj}$ is the luminosity injected into the blast wave (e.g., Zhang et al. 2006). During the deceleration phase, the bulk Lorentz factor in the uniform-density (wind) medium evolves as $\Gamma \propto t^{-\frac{2+q}{8}}(t^{-\frac{q}{2(2-q)}})$. The synchrotron spectral breaks and the maximum flux in the uniform-density (wind) medium become $\epsilon_{\rm m}^{\rm syn} \propto t^{-\frac{2+q}{2}}(t^{-\frac{2+q}{2}})$, $\epsilon_{\rm c}^{\rm syn} \propto t^{\frac{q-2}{2}}(t^{\frac{2-q}{2}})$, and $F_{\rm max} \propto t^{1-q}(t^{-\frac{q}{2}})$, respectively. The predicted synchrotron light curves in the uniform-density (wind) medium for the fast- and slow-cooling regimes are (Zhang et al. 2006)

$$F_\nu^{\rm syn} \propto \begin{cases} t^{\frac{2-3q}{4}}(t^{\frac{2-3q}{4}})\,\epsilon_\gamma^{-\frac{1}{2}}, & \epsilon_{\rm c}^{\rm syn} < \epsilon_\gamma < \epsilon_{\rm m}^{\rm syn}, \\ t^{\frac{2(2-p)-q(p+2)}{4}}(t^{\frac{2(2-p)-q(p+2)}{4}})\,\epsilon_\gamma^{-\frac{p}{2}}, & \epsilon_{\rm m}^{\rm syn} < \epsilon_\gamma, \end{cases} \tag{20}$$

and

$$F_\nu^{\rm syn} \propto \begin{cases} t^{\frac{2(3-p)-q(p+3)}{4}}(t^{\frac{2(1-p)-q(p+1)}{4}})\,\epsilon_\gamma^{-\frac{p-1}{2}}, & \epsilon_{\rm m}^{\rm syn} < \epsilon_\gamma < \epsilon_{\rm c}^{\rm syn}, \\ t^{\frac{2(2-p)-q(p+2)}{4}}(t^{\frac{2(2-p)-q(p+2)}{4}})\,\epsilon_\gamma^{-\frac{p}{2}}, & \epsilon_{\rm c}^{\rm syn} < \epsilon_\gamma, \end{cases} \tag{21}$$

respectively. The injection case due to a millisecond magnetar corresponds to $q = 0$. The standard light curves shown during the deceleration phase in the thin-shell regime (Equations (17) and (18)) are recovered for $q = 1$. For $q > 1$, Equations (20) and (21) are not valid, and the standard light curves apply (Zhang et al. 2006; Lü & Zhang 2014).

3.2.3. Light Curves from Reverse Shocks

To analyze the X-ray/optical flare, we show the predicted synchrotron light curves in the reverse-shock (RS) region before and after the shock-crossing time.

3.2.3.1. Before the Shock-crossing Time

The synchrotron light curves evolving in the uniform-density (wind) medium for the fast- and slow-cooling regimes are (Kobayashi 2000; Fraija et al. 2019b, 2020)

$$F_{\nu,r}^{\rm syn} \propto \begin{cases} t^{\frac{1}{2}}(t^0)\,\epsilon_\gamma^{-\frac{1}{2}}, & \epsilon_{\rm c,\,r}^{\rm syn} < \epsilon_\gamma < \epsilon_{\rm m,\,r}^{\rm syn}, \\ t^{\frac{6p-5}{2}}(t^{\frac{p-1}{2}})\,\epsilon_\gamma^{-\frac{p}{2}}, & \epsilon_{\rm m,\,r}^{\rm syn} < \epsilon_\gamma, \end{cases} \tag{22}$$

and

$$F_{\nu,{\rm r}}^{\rm syn} \propto \begin{cases} t^{\frac{6p-3}{2}}(t^{\frac{p-2}{2}})\,\epsilon_\gamma^{-\frac{p-1}{2}}, & \epsilon_{\rm m,\,r}^{\rm syn} < \epsilon_\gamma < \epsilon_{\rm c,\,r}^{\rm syn}, \\ t^{\frac{6p-5}{2}}(t^{\frac{p-1}{2}})\,\epsilon_\gamma^{-\frac{p}{2}}, & \epsilon_{\rm c,\,r}^{\rm syn} < \epsilon_\gamma, \end{cases} \tag{23}$$

respectively. The subindex r corresponds to the spectral breaks and observed flux in the RS region.

Table 6
The Best-fit Parameters of the XRT Spectrum using a PL and a PL-plus-BB Model

Time Window (s)	$n_{\rm H}\times10^{22}$ ($\rm cm^{-2}$)	Spectral Index β	KT (keV)	Reduced χ^2	$f_{\rm BB}/f_{\rm BL}$
100–150	$0.37^{+0.12}_{-0.10}$	$2.19^{+0.12}_{-0.10}$	⋯	1.19	⋯
	$0.17^{+0.29}_{-0.17}$	$2.10^{+1.80}_{-1.19}$	$0.65^{+0.16}_{-0.11}$	1.16	0.8621
150–200	$0.66^{+0.26}_{-0.20}$	$2.29^{+0.35}_{-0.32}$	⋯	1.24	⋯
	$0.08^{+0.08}_{-0.08}$	-3.00^{+err}_{-err}	$0.67^{+0.07}_{-0.04}$	1.20	2.52
200–230	$1.26^{+0.67}_{-0.49}$	$2.46^{+0.60}_{-0.53}$	⋯	0.76	⋯
	$3.32^{+2.2}_{-1.5}$	$-3.39^{+1.06}_{-0.46}$	$0.07^{+0.01}_{-0.02}$	0.75	389.27
250–299	$1.97^{+1.21}_{-0.92}$	$3.02^{+1.13}_{-0.97}$	⋯	0.95	⋯
	$3.49^{+3.05}_{-2.55}$	5.61^{+err}_{-err}	$1.76^{+1.24}_{-0.95}$	0.96	0.001
300–499	$1.25^{+0.38}_{-0.32}$	$2.64^{+0.44}_{-0.41}$	⋯	1.13	⋯
	$1.40^{+1.32}_{-0.92}$	$3.63^{+3.03}_{-3.38}$	$0.86^{+95.5}_{-0.64}$	1.16	0.07
500–700	$1.00^{+0.35}_{-0.29}$	$2.58^{+0.47}_{-0.44}$	⋯	0.80	⋯
	$1.52^{+0.97}_{-0.92}$	$4.69^{+1.95}_{-2.57}$	$0.92^{+0.81}_{-0.34}$	0.76	0.02
700–900	$1.37^{+0.43}_{-0.36}$	$2.55^{+0.42}_{-0.39}$	⋯	1.36	⋯
	$1.07^{+1.07}_{-0.77}$	$2.32^{+2.83}_{-2.72}$	$0.63^{+0.26}_{-0.19}$	1.34	0.18
1000–1200	$0.91^{+0.14}_{-0.13}$	$2.05^{+0.16}_{-0.15}$	⋯	1.15	⋯
	$0.91^{+0.31}_{-0.30}$	$2.17^{+0.64}_{-1.03}$	$1.16^{+0.91}_{-0.24}$	1.15	0.01
1200–1299	$0.79^{+0.12}_{-0.12}$	$1.87^{+0.14}_{-0.13}$	⋯	1.16	⋯
	$0.94^{+0.18}_{-0.16}$	$1.98^{+0.16}_{-0.15}$	$0.05^{+0.01}_{-0.01}$	1.14	14.76
1300–1399	$0.98^{+0.13}_{-0.12}$	$2.08^{+0.14}_{-0.13}$	⋯	1.19	⋯
	$0.49^{+0.33}_{-0.24}$	$1.29^{+0.66}_{-1.31}$	$0.63^{+0.11}_{-0.08}$	1.19	0.53
1400–1500	$1.09^{+0.15}_{-0.14}$	$2.21^{+0.15}_{-0.14}$	⋯	1.24	⋯
	$0.43^{+0.32}_{-0.18}$	$1.05^{+0.79}_{-1.59}$	$0.64^{+0.07}_{-0.07}$	1.19	0.91
1500–1599	$0.93^{+0.13}_{-0.11}$	$2.05^{+0.13}_{-0.13}$	⋯	1.44	⋯
	$0.73^{+0.26}_{-0.25}$	$1.71^{+0.56}_{-0.60}$	$0.51^{+0.28}_{-0.24}$	1.44	0.16
1600–1700	$1.20^{+0.15}_{-0.14}$	$2.20^{+0.14}_{-0.14}$	⋯	1.26	⋯
	$0.88^{+0.33}_{-0.34}$	$1.79^{+0.48}_{-0.87}$	$0.59^{+0.37}_{-0.11}$	1.30	0.23

Note. The first line in each time window corresponds to the best-fit parameters with the PL and the second with the PL-plus-BB model.

3.2.3.2. After the Shock-crossing Time

The synchrotron light curves evolving in the uniform-density (wind) for the fast and slow-cooling regimes are

$$F^{\rm syn}_{\nu,r}\propto\begin{cases}t^{\frac{-32}{35}}(t^{\frac{-11}{14}})\,\epsilon_\gamma^{-\frac{1}{2}}, & \epsilon^{\rm syn}_{\rm c,\,r}<\epsilon_\gamma<\epsilon^{\rm syn}_{\rm m,\,r},\\ t^{-\frac{27p+5}{35}}(t^{-\frac{2-13p}{14}})\,\epsilon_\gamma^{-\frac{p}{2}}, & \epsilon^{\rm syn}_{\rm m,\,r}<\epsilon_\gamma,\end{cases}\quad(24)$$

and

$$F^{\rm syn}_{\nu,r}\propto\begin{cases}t^{-\frac{27p+7}{35}}(t^{-\frac{39p+7}{42}})\,\epsilon_\gamma^{-\frac{p-1}{2}}, & \epsilon^{\rm syn}_{\rm m,\,r}<\epsilon_\gamma<\epsilon^{\rm syn}_{\rm c,\,r},\\ t^{-\frac{27p+5}{35}}(t^{-\frac{2-13p}{14}})\,\epsilon_\gamma^{-\frac{p}{2}}, & \epsilon^{\rm syn}_{\rm c,\,r}<\epsilon_\gamma,\end{cases}\quad(25)$$

respectively.

3.3. Theoretical Interpretation

3.3.1. The Initial Gamma-ray Pulse and the X-ray Precursor

The initial gamma-ray pulse is fitted with an exponential function $\propto\exp\left(-\frac{t}{\tau_2}\right)$ with $\tau_2=0.39\pm0.10$ s. To interpret these observations, we discuss different scenarios, such as (i) radiation from an expanding cocoon, (ii) synchrotron emission from FSs, (iii) radiation from a relativistic shock breakout, and (iv) emission from internal energy dissipation of the magnetar spin-down power.

3.3.1.1. Radiation from an Expanding Cocoon

Pe'er et al. (2006) showed that fluxes varying as $t^{-\alpha}$ with $\alpha\approx2.5$–4 could be interpreted as the thermal emission from the expanding cocoon once the jet has broken through the stellar envelope. In a multicolor BB scenario (Ryde & Pe'er 2009), with photons emitted from different angles and distinct Doppler boosting, the flux of a thermal spectrum decays as $\propto t^{-2}$. Given that we do not observe the thermal emission in the GBM and BAT data,[15] we discard the idea that this scenario could have produced the X-ray precursor and initial gamma-ray pulse.

[15] For BAT analysis, see https://gcn.gsfc.nasa.gov/notices_s/922968/BA.

3.3.1.2. Synchrotron Emission from FSs

O'Brien et al. (2006) presented the early X-ray observations for 40 bursts using Swift data from BAT and XRT. They proposed that the prompt and the afterglow emission could describe the X-ray light curves. Huang et al. (2018) systematically investigated single-pulse GRBs in the Swift era. The authors found that the prompt emission in a small fraction of bursts could be explained by synchrotron emission from FSs. Some authors have suggested that the synchrotron FS model can explain a single smooth peak or temporally separated peaks during the prompt emission (Dermer & Mitman 2004; McMahon et al. 2004; Golkhou & Butler 2014; Burgess et al. 2016). Concerning GRB 190829A, the initial gamma-ray pulse fits much better with the Band than the CPL function and the BAT observations with the PL than the CPL for a photon index of $\Gamma_{\rm x}=\beta_{\rm x}+1=3.23$. Although the peak energy evolves as $\propto t^{-\frac{3}{2}}$, similar to the characteristic spectral break of the synchrotron FS model when the outflow decelerates in a uniform-density or wind medium, the atypical value of the spectral index $p\approx 5.5$ disagrees with this model ($\beta_{\rm x}=\frac{p-1}{2}$; Sari et al. 1998). Therefore, we discard that the synchrotron FS emission can explain the X-ray precursor and the initial gamma-ray pulse.

3.3.1.3. Radiation from a Relativistic Shock Breakout

Nakar & Sari (2012) computed the luminosity, light curve, and spectrum generated by a relativistic breakout, then the planar phase, and, finally, the spherical phase. They found that spherical relativistic breakouts produce a gamma-ray flash with an energy, temperature, duration, and Lorentz factor that are well defined and related to each other. Besides, they reported that the predicted flux between the planar and spherical relativistic phase evolves as $\propto t^{-2}$ due to the curvature effect (delayed photons arriving from high latitudes). Although the evolution of the flux due to the curvature effect is equal to the initial gamma-ray pulse, we do not observe thermal emission in the GBM and BAT data. Therefore, we discard that the radiation emitted from a relativistic shock breakout can explain the early X-ray precursor and the initial gamma-ray pulse.

3.3.1.4. Emission from Internal Energy Dissipation of the Magnetar Spin-down Power

The initial gamma-ray pulse and the X-ray precursor track the electromagnetic spin-down luminosity with energy dissipation and emission efficiency constant. Considering the case of $r_{\rm c}\ll r_{\rm m}$ and a timescale much less than the characteristic fallback time, Equation (4) becomes

$$\frac{d\Omega}{dt}+\left(\frac{\mu^2}{c^3 I r_{\rm m}^2}+\frac{\dot{M}\,r_{\rm m}^2}{I}\right)\Omega=0, \tag{26}$$

which has as a solution $\Omega\propto\exp\left(-\frac{t}{2t_{\rm sd}}\right)$, where $t_{\rm sd}=\frac{1}{2}\left(\frac{\mu^2}{c^3 I r_{\rm m}^2}+\frac{\dot{M}\,r_{\rm m}^2}{I}\right)^{-1}$. From the evolution of angular frequency, the electromagnetic spin-down luminosity becomes

$$L_{\rm sd}\propto\exp\left(-\frac{t}{t_{\rm sd}}\right), \tag{27}$$

which has a similar profile to the best-fit curve found for these observations. Considering the typical values $B=10^{16}$ G, $P=10^{-3}$ s, and $\dot{M}=10^{-2}\,M_{\odot}$ s^{-1}, the characteristic timescale is $t_{\rm sd}\approx 2.25$ s. Equation (27) agrees with the best-fit curve of the initial gamma-ray pulse and the X-ray precursor.

3.3.2. The X-Ray Plateau Phase

A PL describes the X-ray light curve at 1 keV with a spectral index 0.06 ± 0.03 that is consistent with the "plateau" phase. To explain this phase, we discuss different scenarios, such as (i) synchrotron emission from refreshed shocks, (ii) synchrotron FS emission during the thick-shell regime, and (iii) emission from internal energy dissipation of the magnetar spin-down power.

3.3.2.1. Synchrotron Emission from Refreshed Shocks

A plausible explanation of the plateau phase is that there is a continuous energy injection into the external shock. We identify two possibilities for refreshed shocks: (i) an instantaneous injection with a PL distribution of velocities and (ii) long-lived central-engine activity.

In the first possibility, the instantaneous energy release consists of ejected mass moving with a wide range of Lorentz factors given by $M(>\Gamma)\propto\Gamma^{-\alpha_\Gamma}$ (Tan et al. 2001). The bulk Lorentz factor in the uniform-density (wind) medium evolves as $\Gamma\propto t^{-\frac{3}{\alpha_\Gamma+7}}$ ($t^{-\frac{1}{\alpha_\Gamma+3}}$), and the predicted flux generated by synchrotron emission evolves as $F_\nu^{\rm syn}\propto t^{-\frac{3(2p-\alpha_\Gamma-1)}{7+\alpha_\Gamma}}$ ($t^{-\frac{5p+p\alpha_\Gamma-\alpha_\Gamma-1}{2(7+\alpha_\Gamma)}}$) for $\epsilon_{\rm m}^{\rm syn}<\epsilon_\gamma<\epsilon_{\rm c}^{\rm syn}$ and $F_\nu^{\rm syn}\propto t^{-\frac{2(3p-\alpha_\Gamma-1)}{7+\alpha_\Gamma}}$ ($t^{-\frac{5p+p\alpha_\Gamma-2\alpha_\Gamma-2}{2(3+\alpha_\Gamma)}}$) for $\epsilon_{\rm c}^{\rm syn}<\epsilon_\gamma$ (e.g., see Sari & Mészáros 2000; Zhang et al. 2006; Barniol Duran et al. 2015; Fraija et al. 2019d). To reproduce the plateau phase for a typical value of $p=2.2$, the values of PL indices $\alpha_\Gamma\approx 3.4$ (≈ -8) for $\epsilon_{\rm m}^{\rm syn}<\epsilon_\gamma<\epsilon_{\rm c}^{\rm syn}$ and $\alpha_\Gamma\approx 5.9$ (≈ -42) for $\epsilon_{\rm c}^{\rm syn}<\epsilon_\gamma$ have to be required for the uniform-density (wind) medium. Due to the atypical values required for the wind medium, we discard it.

In the second possibility, the central-engine activity could be due to continuous fallback into the black hole or a millisecond magnetar wind. A continuous luminosity of the central engine can be described by Equation (19), where the electromagnetic spin-down luminosity is injected into the afterglow blast wave (i.e., $L_{\rm inj}=\eta L_{\rm sd}$, with $L_{\rm sd}$ defined by Equation (28) and η an efficiency parameter). The evolution of the Lorentz factor and the predicted flux in the uniform-density (wind) medium are described in Section 3.2.2. To reproduce the plateau phase for a typical value of $p=2.2$, the values of the PL indices $q\approx 0.3$ (≈ -0.8) for $\epsilon_{\rm m}^{\rm syn}<\epsilon_\gamma<\epsilon_{\rm c}^{\rm syn}$ and $q\approx -0.2$ (≈ -0.1) for $\epsilon_{\rm c}^{\rm syn}<\epsilon_\gamma$ are obtained for the uniform-density (wind) medium.

In both types of refreshed-shock models, the synchrotron light curves at the X-ray and optical bands are normalized at $\epsilon_\gamma=1$ keV and $\sim$(1–3) eV, respectively. Therefore, the predicted optical fluxes must be much larger than the X-ray flux ($F_{\nu,{\rm opt}}/F_{\nu,{\rm X}}\gg 1$) for typical values of parameters. However, during this phase, the observed fluxes in the white and U bands are less than the observed X-ray flux. We discard the synchrotron FS emission from refreshed shocks as the origin of the plateau phase.

3.3.2.2. Synchrotron FS Emission during the Thick-shell Regime

From Equations (15) and (16), it can be seen that the synchrotron FS model evolving in a uniform-density medium can describe these observations for $p=3.2\pm0.2$ ($F_\nu\propto t^{0.1\pm0.1}$; $\epsilon_{\rm m}^{\rm syn}<\epsilon_\gamma<\epsilon_{\rm c}^{\rm syn}$), $p=2.1\pm0.2$

($F_\nu \propto t^{0.05\pm0.10}$; $\epsilon_c^{\rm syn} < \epsilon_\gamma$), and, in the wind medium, $p = 1.3 \pm 0.2$ ($F_\nu \propto t^{0.1\pm0.1}$; $\epsilon_m^{\rm syn} < \epsilon_\gamma < \epsilon_c^{\rm syn}$). Taking into account that the observed X-ray flux is larger than the flux in the white and U bands (as discussed in the previous subsection), we discard the synchrotron FS emission during the thick-shell regime as the origin of the plateau phase.

3.3.2.3. Emission from Internal Energy Dissipation of the Magnetar Spin-down Power

Once the system reaches equilibrium ($r_c = r_m$), the accretion term is zero ($N_{\rm acc} = 0$); therefore, the electromagnetic spin-down luminosity becomes $L_{\rm sd} = \Omega N_{\rm dip}$. From Equations (2) and (5), the electromagnetic spin-down luminosity is

$$L_{\rm sd} \simeq \frac{\mu^2\,\Omega_{\rm eq}^4}{c^3}\frac{r_{\rm lc}^2(\Omega_{\rm eq})}{r_c^2} \propto \begin{cases} t^0 & t \ll t_{\rm fb}, \\ t^{-\frac{50}{21}} & t_{\rm fb} \ll t \end{cases}, \quad (28)$$

which, for $t \ll t_{\rm fb}$, is consistent with the best-fit curve during this phase (see Table 4). We conclude that the X-ray light curve tracks the electromagnetic spin-down luminosity with energy dissipation and emission efficiency constant.

Other mechanisms, such as photospheric emission from a moderate outflow injected after the prompt emission (Beniamini & Mochkovitch 2017) and synchrotron FS emission from outflows viewed slightly off-axis (Beniamini et al. 2020), have been recently proposed to interpret the plateau phase. However, we do not observe a photospheric component in this burst, and the $E_{\rm peak}$ and $E_{\rm iso}$ relation indicates that this burst was on-axis (see Section 4.3), so we discard these mechanisms.

3.3.3. A Normal Decay Phase

After the temporal break at $1.4^{+0.17}_{-0.15} \times 10^5$ s, the PL index of the X-ray observations reported was $\alpha_{\rm X,IV} = 1.24 \pm 0.04$.[16] Before this break, a temporal index of $\alpha_{\rm X,IV} = 1.05 \pm 0.02$ is obtained. These observations are consistent with the synchrotron FS model evolving in the uniform-density medium for $p \approx 2.3$. During this phase, the evolution of the hardness ratio shows a moderate spectral softening.

Spectral analysis at 1.8×10^4 s indicates that the X-ray and optical observations evolve in the same PL function with a spectral index of $\beta_{\rm X\cdot O} = 0.47 \pm 0.09$. This value is consistent with the synchrotron model in the range $\epsilon_m^{\rm syn} < \epsilon_\gamma < \epsilon_c^{\rm syn}$ for $p = 1.98 \pm 0.05$. Otherwise, we obtain an atypical value of p, where X-ray and optical observations would evolve in distinct ranges.

Taking into account the temporal and spectral analysis (the closure relations given by Equation (18)), we show that this phase is consistent with the synchrotron FS model that evolves in the uniform-density medium for $p = 2.15 \pm 0.17$. The value of p is consistent with the range of values reported for GRB afterglows (Kumar & Zhang 2015).

3.3.4. The X-Ray and Optical Flares

The X-ray and optical flares coincided, peaking at $\sim 1.4 \times 10^3$ s with rising and falling slopes of ≈ -3 and ≈ 1, respectively. In what follows, we discuss as possible scenarios (i) the synchrotron radiation of late internal shocks due to late central-engine activity, (ii) synchrotron radiation associated with neutron-rich shocks, (iii) synchrotron RS emission, and (iv) synchrotron FS emission.

3.3.4.1. Synchrotron Radiation of Late Internal Shocks

In the fireball model, faster shells in an emitting region of the jet interact with slower ones. If the comoving magnetic field is random or transverse, the synchrotron light curve in the fast-cooling regime would evolve as $t^{-\alpha}$ with $\alpha = 2(p+1)$ or $\frac{2-3p}{2}$, respectively, for $\beta = \frac{p}{2}$ and in the slow-cooling regime with $\alpha = 2p$ or $\frac{1-3p}{2}$, respectively, for $\beta = \frac{1-p}{2}$. Given the best-fit values of the falling slopes of the X-ray and optical flares (see Tables 3 and 4), an atypical value of $p < 1$ would have to be required to reproduce these flares. Considering the simultaneity of the X-ray and optical flares and that the best-fit values of the timescale lie in the range 0.68–1.01, synchrotron radiation of internal shocks created by late central-engine activity cannot reproduce the features of these flares.

3.3.4.2. Synchrotron Radiation Associated with Neutron-rich Shocks

A relevant process that could describe the X-ray and optical flares is synchrotron radiation associated with the presence of neutrons in the outflow (Derishev et al. 1999; Fraija 2014). It occurs as neutrons and ions fully decouple; neutrons create a leading front, and ions start to slow down. Then, neutrons decay in products that interact with the slow-moving ions, producing a rebrightening in the light curve (Beloborodov 2003). Fan & Wei (2004) introduced an analytic formalism to derive the light curves and spectrum. The authors showed that the resulting light curve initially increases fast, then there comes a flat phase, and finally, it drops sharply. Although the light curve exhibited by this scenario has a similar profile to those displayed in GRB 190829A, it occurs at early times comparable with the duration of the burst ($\sim T_{90}$). Given that the X-ray and optical flares peak at $\sim 1.4 \times 10^3$ s, we conclude that synchrotron radiation associated with neutron-rich shocks cannot describe the X-ray and optical flares exhibited in GRB 190829A.

3.3.4.3. Synchrotron RS Emission

The synchrotron RS model is usually required to describe X-ray and optical flares (Kobayashi 2000; Fraija et al. 2016, 2017b; Fraija & Veres 2018). From Equations (22)–(25), it can be seen that before and after the shock-crossing time, the synchrotron RS model evolving in the uniform-density medium could describe the temporal and spectral observations, but for an atypical value of $p \approx 1.3 \pm 0.2$. Besides, the X-ray and optical fluxes are simultaneous during more than $\sim 10^4$ s with similar slopes, so that the synchrotron RS scenario is disfavored. It is worth noting that the predicted synchrotron light curves evolving in a wind medium cannot explain the rising slopes.

3.3.4.4. Synchrotron FS Emission

At early times, the optical and X-ray light curves show bright simultaneous flares peaking at $\sim 1.4 \times 10^3$ s with variability timescales in the range of $\Delta t/t \approx 0.68$–0.9. Tables 3 and 4 show that during the time interval $\sim (0.65$–$1.4) \times 10^3$ s, the X-ray and optical fluxes increase as $t^{-\alpha}$ with slopes of ≈ -3, reaching a maximum flux at $\sim 1.4 \times 10^3$ s. The closure relations during the early afterglow/coasting phase (Equations (13) and

[16] https://www.swift.ac.uk/xrt_live_cat/00922968/

(14)) indicate that the synchrotron FS model in the slow-cooling regime ($\epsilon_{\rm m}^{\rm syn} < \epsilon_\gamma < \epsilon_{\rm c}^{\rm syn}$) and evolving in the uniform-density medium could describe these observations. In the deceleration phase, the synchrotron light curves decrease as $t^{-\alpha}$ with $\alpha \approx 1$ for $p = 2.3$, which is consistent once the X-ray and optical fluxes begin to decrease (see Equations (17) and (18)). On the other hand, spectral analyses at 6×10^3 and 1.8×10^4 s indicate that the X-ray and optical observations evolve in the same PL function with a spectral slope of $\beta_{X\cdot O} = 0.48 \pm 0.05$ and 0.47 ± 0.09, respectively. These values are consistent with the synchrotron FS model in the slow-cooling regime $\epsilon_{\rm m}^{\rm syn} < \epsilon_\gamma < \epsilon_{\rm c}^{\rm syn}$ for $p \approx 2$.

Finally, the temporal and spectral analysis indicates that synchrotron FS emission for $p \approx 2.15 \pm 0.17$ can theoretically describe the X-ray and optical flares.

It is worth noting that photospheric emission emitted at the same time as the material producing the prompt leads to much weaker flares in the optical compared to X-rays, so it may not be appropriate here (Beniamini & Kumar 2016).

3.4. Modeling the Multiwavelength Light Curves

We can obtain the X-ray luminosity using the electromagnetic spin-down luminosity and the efficiency in converting its spin-down energy to radiation ($\eta_{\rm x}$). The X-ray luminosity is given by

$$L_{\rm x} = \eta_{\rm x}\, L_{\rm sd}. \tag{29}$$

Similarly, considering the typical energy range of Swift XRT and the photon spectral index for GRB 190829A, the X-ray luminosity could be converted to X-ray flux using the relationship $F_{\rm x} \simeq \frac{L_{\rm x}}{4\pi d_z^2}$. The term d_z corresponds to the luminosity distance, which is estimated using the values of the Hubble constant as $H_0 = (67.4 \pm 0.5)$ km s^{-1} Mpc^{-1} and the matter density parameter as $\Omega_{\rm m} = 0.315 \pm 0.007$ (Planck Collaboration et al. 2020).

The upper panels in Figure 3 show the X-ray (BAT and XRT) light curve at the (0.3–10) keV energy range with the best-fit curve given by emission from internal energy dissipation of the spin-down magnetar model (left) and the evolution of the Alfvén ($r_{\rm m}$), corotation ($r_{\rm c}$), and light cylinder ($r_{\rm lc}$) radii (right). The fit was done using the MINUIT algorithm (James & Roos 1975) via the `iminuit`[17] Python interface. We use the interpolation of the solution using the `interp1d` function from the `scipy.interpolate` Python object and the χ^2 regression function with the `Chi2Regression` object from the `probfit` Python interface. We place a set of initial values to minimize the function with the `iminuit` interface and the `migrad` optimizer. We assume a fallback mass of $M_{\rm fb} = 0.8\ M_\odot$ (Metzger et al. 2018) and $\eta_{\rm x} = 0.1$ (Bernardini et al. 2013; Xiao & Dai 2019). We report the best-fit values of the magnetic field, spin period, and fallback timescale in Table 7. This panel shows the evolution of the magnetization parameter (below). This parameter lies in the range of $100 \lesssim \sigma \lesssim 3000$ in the intervals [0.1; 7.2] s and [78.5; 7.6 $\times$ 10^4] s. These time intervals coincide with the X-ray precursor, and the X-ray peaks at 15–50 keV. The inset in the upper left panel shows the X-ray light curve at the (15–50) keV energy range (above) and the evolution of the magnetization parameter (below). During the early X-ray observations, the extracted rotational energy is 4.18×10^{50} erg, and during the plateau phase, it is 2.93×10^{47} erg. Comparing the extracted rotational energy associated with the precursor with the isotropic-equivalent energy (see Table 1), we can estimate an efficiency of $(21.7 \pm 1.13)\%$. The upper right panel shows that the spin period reaches its equilibrium at ~ 10 s (on a timescale of $\sim 10^{-2}\, t_{\rm fb}$). During the first seconds, the light cylinder radius is less than the Alfvén radius, so the electromagnetic spin-down luminosity is similar to the isolated magnetar. The system lies in the propeller regime so that the angular momentum losses decrease the total rotational energy.

The lower panel shows the multiwavelength light curves of GRB 190829A, with the best-fit curves given by emission from internal dissipation of the magnetar spin-down power and the synchrotron FS model. We show UVOT data at the V band. The quantities observed for GRB 190829A, such as the redshift $z = 0.078$, isotropic-equivalent energy 2.967×10^{50} erg, and spectral index $\Gamma_{\rm x} = 2.2$,[18] are used. The blue line shows the total contribution, and the magenta line shows the synchrotron FS model with the host galaxy contribution. The best-fit values of the uniform-density medium (n), equivalent kinetic energy (E), spectral index (p), and microphysical parameters given to accelerate electrons ($\varepsilon_{\rm e}$) and amplify the magnetic field ($\varepsilon_{\rm B}$) during the FSs are reported in Table 7. Given the parameters found, we can estimate (i) the value of the initial bulk Lorentz factor as $\Gamma \simeq 34$, which is low for hlGRBs and high for llGRBs (Schulze et al. 2014); (ii) the deceleration radius at the peak time (1.4×10^3 s) of the afterglow as $R_{\rm dec} \simeq 0.05$ pc; (iii) the efficiency to convert the kinetic energy into photons as $\eta_{\rm k} = 12.4\%$, which is typical for GRB afterglows (Kumar & Zhang 2015; Beniamini et al. 2015); and (iv) the spectral break energies as $\epsilon_{\rm m}^{\rm syn} = 1.9$ eV and $\epsilon_{\rm c}^{\rm syn} = 0.1$ MeV, which indicate that the synchrotron model evolves in the slow-cooling regime.

Based on the analysis and modeling of the multiwavelength observations, we present a full discussion of GRB 190829A.

4. Results and Discussion

4.1. Nonexistence of the Thermal Emission

The thermal emission is expected during the precursor and main emission episode in the framework of the photosphere, shock breakout, and cocoon models. For GRB 190829A, the Band function better fits the GBM data (the initial pulse and brighter peak) than the BB function, and the PL function fits the BAT data better than the BB function.[19] The nondetection of thermal emission in both the GBM and BAT data indicates that the GRB outflow might carry a significant fraction of the magnetic field (Zhang & Pe'er 2009; Gao & Zhang 2015) or the Band function is the result of the reprocessed quasi-thermal emission from kinetical or magnetic dissipation processes near the photosphere (Pe'er et al. 2006; Lazzati & Begelman 2010; Vurm et al. 2011; Veres et al. 2012; Lundman et al. 2013; Ahlgren et al. 2015; Vurm & Beloborodov 2016). The detection of a single nonthermal emission, as well as the evolution of the spectral parameters (see Section 2.2.1.1), would favor the scenario of a Poynting flux–dominated outflow (Zhang & Pe'er 2009; Beniamini & Piran 2014; Gao & Zhang 2015).

[17] https://github.com/scikit-hep/iminuit

[18] https://www.swift.ac.uk/xrt_spectra/00922968/

[19] For BAT analysis, see https://gcn.gsfc.nasa.gov/notices_s/922968/BA.

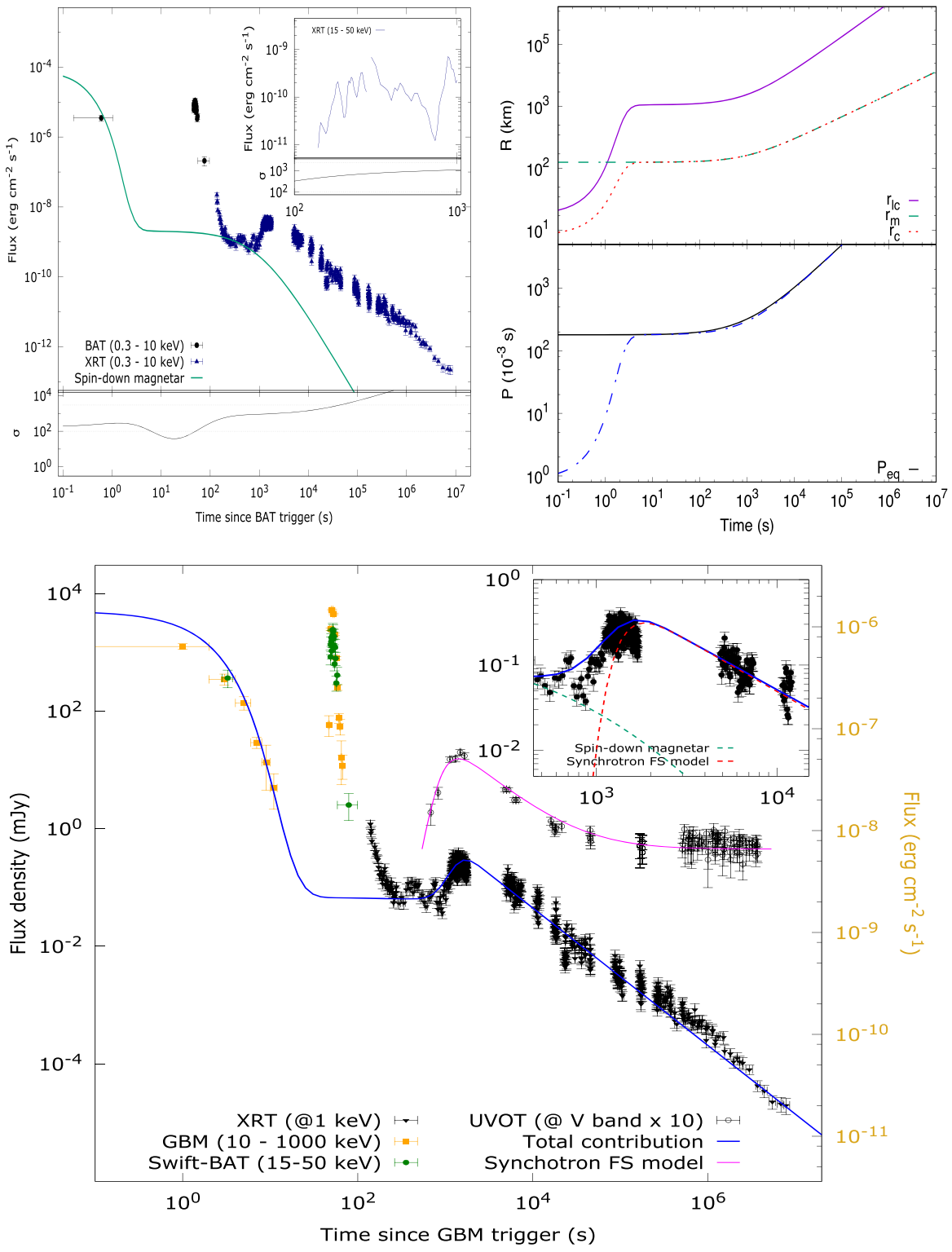

Figure 3. The upper left panel shows the X-ray light curve, with the best-fit curve given by the emission from the internal energy dissipation of the spin-down magnetar model (above) and the evolution of the magnetization parameter (below). The inset shows the light curve at 10 keV. The upper right panel shows the evolution of the Alfvén (r_m), corotation (r_c), and light cylinder (r_{lc}) radii (above) and the evolution of the spin period (below). The lower panel shows the multiwavelength light curves of GRB 190829A with the best-fit curves from the emission from internal dissipation of the magnetar model and the synchrotron FS model.

4.2. Analysis of the GRB Tail Emission

The GRB tail emission marks the end of the prompt phase and the onset of the afterglow (Zhang et al. 2006). This emission reveals whether the prompt emission and the afterglow originate from distinct components or emitting sites. If the prompt emission and the afterglow arise from distinct components or emission sites, we should observe an abrupt

Table 7
The Best-fit Parameters Found from the Multiwavelength Observations

Parameter	Values
Spin-down magnetar	
B ($\times 10^{16}$ G)	6.0 ± 0.3
P (10^{-3} s)	1.1 ± 0.1
$t_{\rm fb}$ (s)	$(9.5 \pm 0.8) \times 10^2$
Synchrotron FS model	
$\varepsilon_{\rm B}$ (10^{-4})	1.1 ± 0.1
$\varepsilon_{\rm e}$ (10^{-1})	0.8 ± 0.1
p	2.3 ± 0.2
n (10^{-1} cm^{-3})	1.0 ± 0.1
E (10^{51} erg)	2.4 ± 0.2

decay in the flux level during the transition phase between the prompt emission and the afterglow. Such abrupt decay, which accounts for the delayed photons, is associated with the high-latitude emission due to the curvature effect (Kumar & Panaitescu 2000). During the interval, 82 s $\lesssim t \lesssim$ 215 s, the X-ray light curve at 1 keV exhibited a fast decay, which is difficult to explain by invoking the external shock model. Some authors have argued that central engines cannot die suddenly and that the observed GRB tails may account for the central engines' dying history (Fan & Wei 2005; Barniol Duran & Kumar 2009). Given the best-fit value of the steep decay $\alpha_{X,I} = 3.53 \pm 0.70$ and the large variation exhibited by the spectral index and hardness ratio, we can interpret the X-ray observations in GRB 190829A during this epoch in the context of the high-latitude emission for $p = 3.06 \pm 1.40$ (Kumar & Panaitescu 2000). As seen in other bursts detected by Swift (Goad et al. 2007), a temporal analysis shows a high correlation between the photon index and source intensity, with the spectrum being harder when brighter. This result indicates that the steep decay observed in the Swift XRT data is connected with the prompt emission (Barthelmy et al. 2005; Tagliaferri et al. 2005).

Given the GRB tail emission, the opening angle for a canonical jet is

$$\theta_j \approx 8^\circ \left(\frac{1+z}{1.08}\right)^{-\frac{1}{2}} t_{\rm tail,\,2}^{\frac{1}{2}}\, R_{\rm cr,14.5}^{-\frac{1}{2}}, \quad (30)$$

where $t_{\rm tail}$ is the duration of the tail, and $R_{\rm cr}$ is the curvature radius. Using the value of the opening angle, we calculate the initial bulk Lorentz factor $\Gamma \gtrsim 25 \frac{t_{\rm tail,\,2}^{\frac{1}{2}}}{\sqrt{1-\cos\theta_j}}$, which is consistent with the value estimated from the peak time of the afterglow.

Before and after the GRB tail emission, we identify the prompt emission and afterglow, respectively. A rough comparison between the X-ray emission level during the prompt emission and the afterglow could indicate if both emissions originated in the same component (Zhang et al. 2006). Given the low-energy spectral index $\alpha_{\rm Band}$, the energy peak and total isotropic energies reported in Table 1, the duration of the burst, the equivalent kinetic energy ($E_{\rm k} = 10^{52}$ erg), the energy at which the X-rays are reported ($E_{\rm X} = 1$ keV), and the microphysical parameter ($\varepsilon_e \approx 0.1$), the flux ratio is (see Zhang et al. 2006)

$$\frac{F_{\nu,{\rm X}}^{\rm pr}}{F_{\nu,{\rm X}}^{\rm ag}} \approx 0.4 \left(\frac{E_{\gamma,{\rm iso},51}}{E_{\rm k,\,52}}\right)\left(\frac{t_2}{T_{90}}\right)\left(\frac{E_{\rm X,1\,keV}}{E_{\rm pk,10\,keV}}\right)^{\alpha_{\rm Band}+2} \varepsilon_{\rm e,-1}^{-1}. \quad (31)$$

This estimate is wholly different from the flux ratio ($>10^4$) observed in GRB 190829A, so we conclude that the prompt emission and the afterglow originate from different components.

4.3. E_{peak}–$E_{\gamma,iso}$ Relation

Using the derived values of the total isotropic energy $(2.967 \pm 0.032) \times 10^{50}$ erg and the peak energy of the gamma-ray spectrum $E_{\rm peak} = 11.47 \pm 0.360$ keV, we found that GRB 190829A is consistent with the $E_{\rm peak}$–$E_{\gamma,{\rm iso}}$ relation (Amati relation; Amati et al. 2002; Amati 2006) as other GRB SNe associated with millisecond magnetars (Cano et al. 2014). Figure 4 shows the $E_{\rm peak}$–$E_{\gamma,{\rm iso}}$ relation for GRBs detected by Konus-Wind, Swift-BAT, and the llGRB, ilGRB, and hlGRB sample within $z \lesssim 0.2$. The best-fit value of the correlation is adapted from D'Elia et al. (2018). The llGRBs, ilGRBs and hlGRBs are obtained from GRB 980425/SN 1998bw (Galama et al. 1998), GRB 060218/SN 2006aj (Campana et al. 2006), GRB 100316D/SN 2010bh (Cano et al. 2011), GRB 161219B/SN 2016jca (Cano et al. 2017; Ashall et al. 2019), GRB 171205A/SN 2017iuk (Izzo et al. 2019), GRB 130702A/SN 2013dx (D'Elia et al. 2015), and GRB 030329/SN 2003dh (Hjorth et al. 2003). It worth noting that GRB 190829A follows this relation, indicating that this burst was not off-axis.

5. Analysis and Discussion of the Multi-GeV Photons

5.1. Synchrotron Limit

Given the best-fit parameters (see Table 7), we plot in the left panel of Figure 5 the evolution of the maximum-energy photon radiated by the synchrotron FS model in the uniform-density medium. In addition, we plot the VHE emission in the range reported by the H.E.S.S. telescopes. The figure shows that the synchrotron FS model cannot explain these VHE photons. Therefore, an additional mechanism should be present during the FSs to explain these multi-GeV photons. It is worth noting that the synchrotron FS model can explain photons at hundreds of MeV below the synchrotron limit (Kumar & Barniol Duran 2009).

Synchrotron photons radiated in the FSs can be upscattered by the same electron population. Here we use the best-fit parameters reported in Table 7 and the SSC FS emission in the uniform-density medium introduced in Fraija et al. (2019a).

5.2. SSC FS Model

Once the jet begins to decelerate, the intrinsic attenuation due to $\gamma\gamma$ interactions[20] can be estimated by (e.g., see Vedrenne & Atteia 2009)

$$\tau_{\gamma\gamma,{\rm in}} \simeq 10^{-1}\, R_{\rm dec,\,17}\, \Gamma_{1.5}^{-1}\, n_{\gamma,10.7}, \quad (32)$$

where $R = 2.7 \times 10^{17}\,{\rm cm}\, n^{-\frac{1}{3}} E_{51.2}^{\frac{1}{3}} \Gamma_{1.5}^{-\frac{2}{3}}$ is the FS radius, and $n_\gamma \simeq 5 \times 10^{10}\,{\rm cm}^{-3}\, L_{\gamma,49}\, R_{\rm dec,\,17}^{-2}\, \Gamma_{1.5}^{-1}\, \epsilon_{\gamma,3}^{-1}$ is the density of

[20] The VHE gamma-ray photons can interact with lower-energy photons to produce pairs.

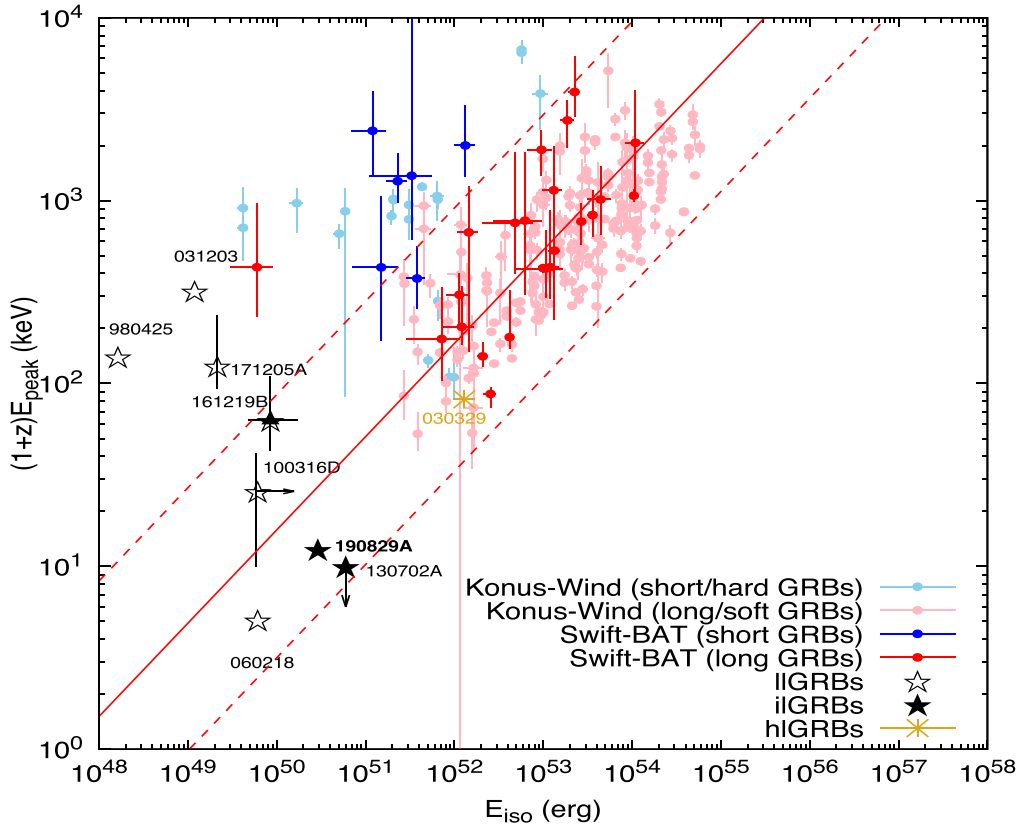

Figure 4. The $E_{\rm peak}$–$E_{\rm iso}$ relation for GRBs detected by Konus-Wind, Swift-BAT, and llGRB samples. This figure is adapted from D'Elia et al. (2018). The black filled star labeled in bold shows GRB 190829A. The solid and dashed red lines correspond to the best-fit curve and vertical logarithmic deviations (2.5σ), respectively, reported in Krimm et al. (2009). The $E_{\rm peak}$ and $E_{\rm iso}$ of llGRBs, ilGRBs, and hlGRBs are obtained from GRB 980425/SN 1998bw (Galama et al. 1998), GRB 060218/SN 2006aj (Campana et al. 2006), GRB 100316D/SN 2010bh (Cano et al. 2011), GRB 161219B/SN 2016jca (Cano et al. 2017; Ashall et al. 2019), GRB 171205A/SN 2017iuk (Izzo et al. 2019), GRB 130702A/SN 2013dx (D'Elia et al. 2015), and GRB 030329/SN 2003dh (Hjorth et al. 2003).

the keV energy photons associated with its photon luminosity. Due to the fact that $\tau_{\gamma\gamma,\rm in}\ll 1$, the intrinsic attenuation is not considered.

The minimum and cooling electron Lorentz factors are

$$\gamma_{\rm m} = 4.3 \times 10^2\,\varepsilon_{\rm e,1.1}\,\Gamma_{1.5},$$
$$\gamma_{\rm c} = 8.4 \times 10^5\left(\frac{1+z}{1.08}\right)[1+Y(\gamma_{\rm c})]^{-1}\,\varepsilon_{B,-4}^{-1}\,n^{-1}\Gamma_{1.5}^{-3}\,t_3^{-1}, \tag{33}$$

where $Y(\gamma_{\rm c})$ corresponds to the Compton parameter of the electrons with Lorentz factor γ_c (Wang et al. 2010). The value of $Y(\gamma_{\rm c})$ is given by

$$Y(\gamma_c) = \frac{\eta\varepsilon_{\rm e}}{\varepsilon_{\rm B}[1+Y(\gamma_c)]}\begin{cases}\left(\dfrac{\epsilon_{\rm KN}(\gamma_{\rm c})}{\epsilon_{\rm c}}\right)^{\frac{3-p}{2}}, & \epsilon_{\rm m}^{\rm syn} < \epsilon_{\rm KN}^{\rm syn}(\gamma_{\rm c}) < \epsilon_{\rm c}^{\rm syn}\\ 1., & \epsilon_{\rm c}^{\rm syn} < \epsilon_{\rm KN}^{\rm syn}(\gamma_{\rm c}),\end{cases} \tag{34}$$

with $\eta = \left(\frac{\gamma_{\rm c}}{\gamma_{\rm m}}\right)^{2-p}$ and $\epsilon_{\rm KN}^{\rm syn}(\gamma_{\rm c}) = \frac{\Gamma\, m_{\rm e}c^2}{\gamma_{\rm c}}$ (Nakar et al. 2009; Wang et al. 2010). Given the synchrotron spectral breaks $\epsilon_{\rm m}^{\rm syn} = 2.9$ eV, $\epsilon_{\rm c}^{\rm syn} = 0.1$ MeV, and $\epsilon_{\rm KN}^{\rm syn}(\gamma_{\rm c}) \simeq 12.8$ eV, the Compton parameter lies in the range of $\epsilon_{\rm m}^{\rm syn} < \epsilon_{\rm KN}^{\rm syn}(\gamma_{\rm c}) < \epsilon_{\rm c}^{\rm syn}$. Solving Equation (34), the value of $Y(\gamma_c)$ becomes ~0.8.

Given the electron Lorentz factors (Equation (33)) and the synchrotron spectral breaks (Sari et al. 1998), the spectral breaks and maximum flux for SSC emission are

$$\epsilon_{\rm m}^{\rm ssc} \simeq 0.1\ {\rm MeV}\left(\frac{1+z}{1.08}\right)^{\frac{5}{4}}\varepsilon_{e,-1.1}^{4}\,\varepsilon_{B,-4}^{\frac{1}{2}}\,n^{-\frac{1}{4}}\,E_{51.2}^{\frac{3}{4}}\,t_3^{-\frac{9}{4}},$$
$$\epsilon_{\rm c}^{\rm ssc} \simeq 6.1 \times 10^5\ {\rm TeV}\left(\frac{1+z}{1.08}\right)^{-\frac{3}{4}}\left(\frac{1+Y_{\rm Th}}{1.8}\right)^{-4} \times \varepsilon_{B,-4}^{-\frac{7}{2}}\,n^{-\frac{9}{4}}\,E_{51.2}^{-\frac{5}{4}},\ t_3^{-\frac{1}{4}},$$
$$F_{\rm max}^{\rm ssc} \simeq 3.2 \times 10^{-5}\ {\rm mJy}\left(\frac{1+z}{1.08}\right)^{\frac{3}{4}}\varepsilon_{B,-4}^{\frac{1}{2}}\,n^{\frac{5}{4}}\,d_{z,27}^{-2}\,E_{51.2}^{\frac{5}{4}}\,t_3^{\frac{1}{4}}. \tag{35}$$

The cooling spectral break is too large in comparison with the Fermi-LAT energy. The SSC light curves in the fast- (slow)-cooling regime are (Fraija et al. 2019a)

$$F_\nu^{\rm ssc} \propto \begin{cases} t^{\frac{1}{8}}\epsilon_\gamma^{-\frac{1}{2}}(t^{-\frac{9p-11}{8}}\epsilon_{\gamma,11}^{-\frac{p-1}{2}}), & \epsilon_{\rm c}^{\rm ssc}(\epsilon_{\rm m}^{\rm ssc}) < \epsilon_\gamma < \epsilon_{\rm m}^{\rm ssc}(\epsilon_{\rm c}^{\rm ssc}),\\ t^{-\frac{9p-10}{8}}\,\epsilon_\gamma^{-\frac{p}{2}}, & \{\epsilon_{\rm c}^{\rm ssc},\,\epsilon_{\rm m}^{\rm ssc}\} < \epsilon_\gamma.\end{cases} \tag{36}$$

The SSC emission must consider the effect of Klein–Nishima (KN) suppression because of the reduction of the emissivity compared with the classical Compton regime. The break

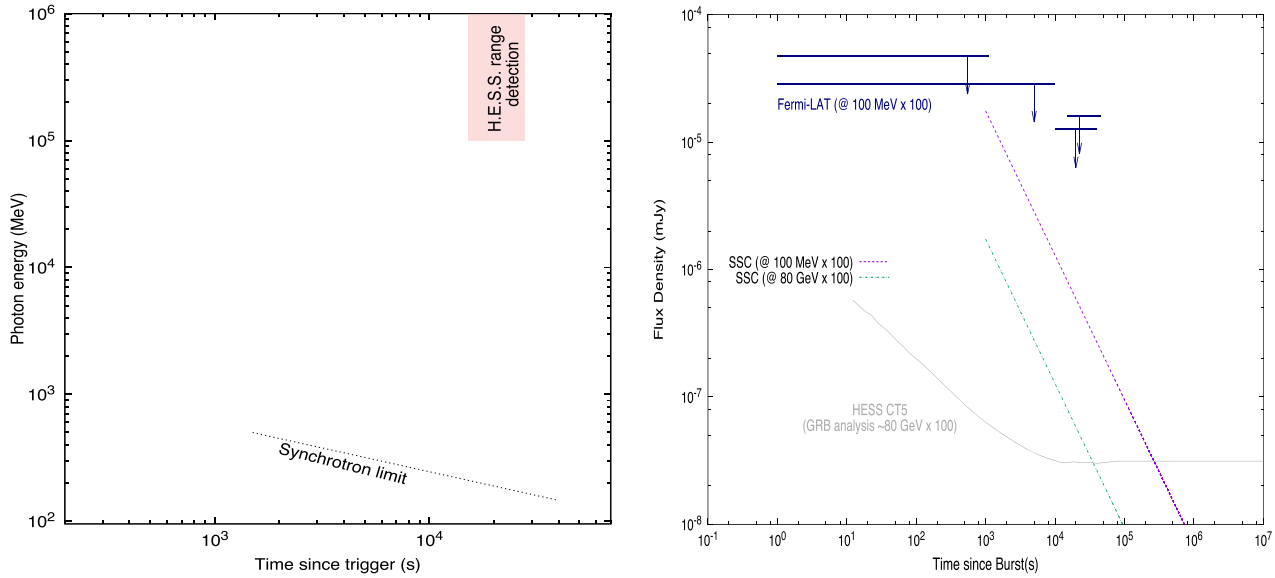

Figure 5. The left panel shows the interval and energy range of VHE photons reported by the H.E.S.S. Collaboration (pink region) and the synchrotron limit (dashed line). The right panel shows the SSC FS emission estimated at 100 MeV and 80 GeV. To verify our model with the observations at high energies and VHEs, we show the Fermi-LAT upper limits at 100 MeV and the sensitivity of H.E.S.S. at 80 GeV (Piron 2016).

energy in the KN regime is

$$\epsilon_{\rm c}^{\rm KN} \simeq 14.3\ {\rm TeV}\left(\frac{1+z}{1.08}\right)^{-\frac{3}{4}}\left(\frac{1+Y_{\rm Th}}{1.8}\right)^{-1}\varepsilon_{B,-4}^{-1}\, n^{-\frac{3}{4}}\, E_{51.2}^{-\frac{1}{4}} \times t_3^{-\frac{1}{4}}. \quad (37)$$

5.3. H.E.S.S. Detection with Fermi-LAT Upper Limits

From the spectral breaks of synchrotron ($\epsilon_{\rm m}^{\rm syn} \simeq 2.9$ eV and $\epsilon_{\rm c}^{\rm syn} \simeq 0.1$ MeV) and SSC ($\epsilon_{\rm m}^{\rm ssc} \simeq 0.1$ MeV and $\epsilon_{\rm c}^{\rm ssc} \simeq 6.1 \times 10^5$ TeV) emission, one can see that at 100 MeV, the synchrotron emission lies in the range $\epsilon_{\rm m}^{\rm syn} < \epsilon_{\rm c}^{\rm syn} < \epsilon_\gamma$, and the SSC emission lies in the range $\epsilon_{\rm m}^{\rm ssc} < \epsilon_\gamma < \epsilon_{\rm c}^{\rm ssc}$. It is important to consider electrons that have electron Lorentz factors $\gamma_{\rm e}^*$ and radiate synchrotron photons at 100 MeV. Using the electron Lorentz factor that produces synchrotron photons at the LAT regime, it is possible to obtain the critical energy $\epsilon_{\rm KN}^{\rm syn}(\gamma_{\rm e}^*) = \frac{\Gamma m_{\rm e} c^2}{\gamma_{\rm e}^*} \simeq 1.4$ eV (Nakar et al. 2009). In this case, the Compton parameter becomes $Y(\gamma_{\rm e}^*) = Y(\gamma_{\rm c})\left(\frac{\epsilon_{\rm KN}^{\rm syn}(\gamma_{\rm e}^*)}{\epsilon_{\rm KN}^{\rm syn}(\gamma_{\rm c})}\right)^{\frac{3-p}{2}} \simeq 0.7$, which corresponds to the range $\epsilon_{\rm KN}^{\rm syn}(\gamma_{\rm e}^*) < \epsilon_{\rm m}^{\rm syn} < \epsilon_{\rm KN}^{\rm syn}(\gamma_{\rm c}) < \epsilon_{\rm c}^{\rm syn}$ (Nakar et al. 2009; Wang et al. 2010; Beniamini et al. 2015).

Therefore, the ratio of synchrotron and SSC fluxes at 100 MeV becomes

$$\frac{F_\nu^{\rm syn}}{F_\nu^{\rm ssc}} \sim 5.1\left(\frac{1+z}{1.08}\right)^{-\frac{1}{4}}\left(\frac{1+Y(\gamma_{\rm e}^*)}{1.7}\right)^{-1}\varepsilon_{e,-1.1}^{1-p}\varepsilon_{B,-4}^{-\frac{3}{4}} n^{-\frac{7}{6}} E_{51.2}^{-\frac{1}{12}} \times \Gamma_{1.5}^{\frac{5}{3}-p} t_3^{-\frac{1}{4}}\left(\frac{\epsilon_\gamma}{100\ {\rm MeV}}\right)^{-\frac{1}{2}}. \quad (38)$$

The ratio of the SSC to synchrotron luminosity is approximately given by $Y(\gamma_{\rm c}) \equiv \frac{L_\nu^{\rm ssc}}{L_\nu^{\rm syn}} = \frac{U_{\rm syn}[\epsilon_\gamma < \epsilon_{\rm KN}^{\rm syn}(\gamma_{\rm c})]}{U_{\rm B}} \simeq 0.8$ (Wang et al. 2010). The terms $U_{\rm B}$ and $U_{\rm syn}[\epsilon_\gamma < \epsilon_{\rm KN}^{\rm syn}(\gamma_{\rm c})]$ are the energy densities of the magnetic field and the synchrotron photons with energy below $\epsilon_{\rm KN}^{\rm syn}(\gamma_{\rm c})$.

The right panel of Figure 5 shows the SSC FS emission estimated at 100 MeV (dashed magenta curve) and 80 GeV (dotted–dashed green curve). We consider the attenuation produced by the extragalactic background light (EBL) absorption following the model presented in Franceschini & Rodighiero (2017). The intrinsic attenuation by $e^\pm$ pair production is not taken into account because it is not significant during the deceleration phase. To verify our model results with the observations at high energies and VHEs, we show the Fermi-LAT upper limits at 100 MeV and H.E.S.S.'s sensitivity at 80 GeV. This panel shows that the SSC emission can reproduce the observations of H.E.S.S. and Fermi-LAT (i.e., the H.E.S.S. telescopes can detect the SSC emission without being detected by the Fermi-LAT instrument).

5.4. Why Was GRB 190829A Detectable at VHEs?

In the following, we enumerate the reasons why the H.E.S.S. telescopes detected this burst.

(i) *A burst located at a very low redshift with an intermediate luminosity.* Depending on the redshift and photon energy, the VHE flux from a generic source begins to be attenuated due to $e^\pm$ pair creation with EBL photons (Gould & Schréder 1966). This attenuation can be measured through $\exp[-\tau_{\gamma\gamma}(z)]$, where $\tau_{\gamma\gamma}(z)$ is the opacity. Considering the low redshift of this burst ($z \simeq 0.078$), the VHE flux at 100 GeV and 1 TeV is attenuated by a factor of 0.99 and 0.44 (Franceschini & Rodighiero 2017), respectively. On the other hand, with the best-fit parameters found after describing GRB 190829A, the SSC flux evolves in the range $\epsilon_{\rm m}^{\rm ssc} < \epsilon_\gamma < \epsilon_{\rm c}^{\rm ssc}$, and consequently, the SSC flux varies as $\propto E^{1.1}$. Therefore, the tiny attenuation factor, together with an intermediate luminosity, allowed that the H.E.S.S. observatory could have detected GRB 190829A. It is worth noting that although no imaging atmospheric Cherenkov telescope (IACT) was observing GRB 130702A, an

intermediate-luminosity burst with $z \lesssim 0.2$, Fermi-LAT detected a GeV photon associated with this burst (see Section 5.6).

(ii) *The VHE emission originated during the deceleration phase.* Fermi-LAT, MAGIC, and H.E.S.S. have reported VHE photons during the prompt and afterglow in tens of bursts (Ajello et al. 2019; Acciari et al. 2019; Abdalla et al. 2019). Different studies of multiwavelength observations have yielded results about the place of VHE flux origin (e.g., internal and external shocks; Kumar & Zhang 2015). Following our model and the best-fit values found, we conclude that the VHE emission had its origin during the deceleration phase with the intrinsic attenuation due to $\gamma\gamma$ interactions much less than unity. In this case, the intrinsic attenuation did not decrease the observed SSC emission.

(iii) *A favorable set of parameters.* The set of best-fit parameters, as found for GRB 190829A, made its detection more favorable. For instance, with the best-fit parameters, the SSC flux evolving in the range $\epsilon_{\rm m}^{\rm ssc} < \epsilon_\gamma < \epsilon_{\rm c}^{\rm ssc}$ increases as the circumburst density ($\propto n^{1.1}$) and electron equipartition parameter ($\propto \varepsilon_{\rm e}^{2.3}$) increase. Higher values of these parameters make SSC emission more favorable to be detected.

(iv) *The KN regime is much above hundreds of GeV.* The KN effects are essential in the SSC flux above 14.3 TeV. They allowed the SSC flux to not remain attenuated below 1 TeV; hence, the H.E.S.S. telescopes could detect VHE photons from GRB 190829A.

(v) *A quick location of this burst.* To observe photons at hundreds of GeV by IACTs has indeed been a difficult challenge, since they take longer in locating the burst than the duration of the prompt emission and early afterglow. Despite numerous attempts, two observations, GRB 180720B (Abdalla et al. 2019) and GRB 190114C (Acciari et al. 2019), have been possible, and these telescopes have derived many upper VHE limits (e.g., see H.E.S.S. Collaboration et al. 1992; Albert et al. 2007; Aharonian et al. 2009a, 2009b; Aleksić et al. 2014; Acciari et al. 2011; Bartoli et al. 2017; Abeysekara et al. 2018). We argue that the conditions to quickly pinpoint the early afterglow of GRB 190829A by the H.E.S.S. telescope made the VHE flux detection possible.

5.5. Analysis of Our SSC Model for Other VHE Observatories

CTA telescopes. Funk et al. (2013) and Piron (2016) presented and discussed the sensitivity to transient sources of the Cherenkov Telescope Array (CTA) for distinct energy thresholds. At 10^3 s, the CTA sensitivity for an energy threshold of 75 GeV is $\sim 2.6 \times 10^{-10}$ mJy. To compare with our SSC model, the corresponding SSC flux, at $t = 10^3$ s and $\epsilon_\gamma = 75$ GeV, is $\simeq 9.0 \times 10^{-9}$ mJy. Hence, we conclude that CTA would have detected GRB 190829A if this had been working. The GRBs with similar characteristics of GRB 190829A are potential candidates to be detected (e.g., CTA; Funk et al. 2013).

MAGIC telescopes. Takahashi et al. (2008) reported the MAGIC GRB sensitivity as a function of time at 100 GeV. At 10^3 s, the MAGIC sensitivity becomes $\sim 10^{-10}$ mJy. The corresponding SSC flux, at $t = 10^3$ s and $\epsilon_\gamma = 100$ GeV, would be $\simeq 7.5 \times 10^{-9}$ mJy. Therefore, we conclude that if this burst had been located early by the MAGIC telescopes, these telescopes would have detected GRB 190829A.

HAWC Observatory. The High Altitude Water Cherenkov (HAWC) collaboration reported the GRB sensitivity as a function of time for distinct zenith angles in the energy range of (0.1–1) TeV (Martinez-Castellanos 2019). Considering the zenith angle with respect to GRB 190829A ($\theta_{\rm zenith} = 30^\circ$) at 10^3 s, the flux sensitivity is around $\simeq 10^{-8}$ erg cm^{-2} s^{-1}. Taking into account the EBL absorption effect in the (0.1–1) TeV energy range, the SSC flux would be $\simeq 10^{-9}$ erg cm^{-2} s^{-1}. We conclude that GRB 190829A could not have been detected by the HAWC gamma-ray observatory, even if this burst would have occurred during the first hours within its field of view.

5.6. Generalization to the Closest ilGRBs ($z \lesssim 0.2$)

To date, there is only one confirmed ilGRB SN detected with $z \lesssim 0.2$: GRB 130702A. It is classified as an intermediate-luminosity burst and associated with the broad-line Type Ic SN 2013dx (D'Elia et al. 2015) and was detected in different wavelengths ranging from radio to high-energy gamma rays. The Fermi GBM instrument triggered on GRB 130702A on 2013 July 2 at 00:05:23.079 UTC. The Fermi-LAT instrument detected photons from this burst above >100 MeV within 2200 s. The duration of the main emission in the (50–300) keV energy range was $T_{90} = 59$ s, and the isotropic energy reported was $6.4^{+1.3}_{-1.0} \times 10^{50}$ erg for a redshift of $z = 0.145$ (Toy et al. 2016).

5.6.1. Fermi-LAT Analysis and Synchrotron Limit

The left panel in Figure 6 displays the Fermi-LAT energy flux (blue) and photon flux (red) light curves and upper limits obtained between 0.1 and 100 GeV. This panel shows that the flux at $\sim 10^3$ s is slightly above the upper limits at $>10^4$ s.

The right panel in Figure 6 shows high-energy photons (>100 MeV) with their corresponding probabilities of being associated with GRB 130702A. The data files used for this analysis are at the data website.[21] We analyze Fermi-LAT data using the Fermi tools and the procedure presented in Fraija et al. (2019c). We note several features: (i) Fermi-LAT detected three high-energy photons with probabilities >90% of 1661, 540, and 464 MeV detected at 272, 1070, and 1818 s, respectively, after the trigger time; (ii) the highest-energy photon of 1661 MeV corresponded to the first photon observed at 272 s; and (iii) this burst displayed five photons above >100 MeV with a probability of less than 10% (the highest-energy photon was 7 GeV).

Taking into account the value of the circumburst density $n = 1$ cm^{-3}, the total isotropic-equivalent energy $6.4^{+1.3}_{-1.0} \times 10^{50}$ erg (D'Elia et al. 2015), the redshift of $z = 0.145$ (Toy et al. 2016), and the efficiency to convert the kinetic energy into photons 0.2 (Beniamini et al. 2015), we estimate and plot the evolution of the maximum-energy photon radiated by the synchrotron FS model, as shown in the right panel in Figure 6. This panel shows that the synchrotron FS scenario cannot explain Fermi-LAT's highest-energy photon. Therefore, as concluded for GRB 190829A, an additional mechanism, such as SSC emission, should be present during the FSs to explain this GeV energy photon.

5.6.2. Parameter Space So that the H.E.S.S. Telescopes Can Detect VHE Photons from ilGRBs

Using the SSC FS model (Equations (35) and (36)), we compute the parameter space so that the H.E.S.S. telescopes

[21] https://fermi.gsfc.nasa.gov/cgi-bin/ssc/LAT/LATDataQuery.cgi

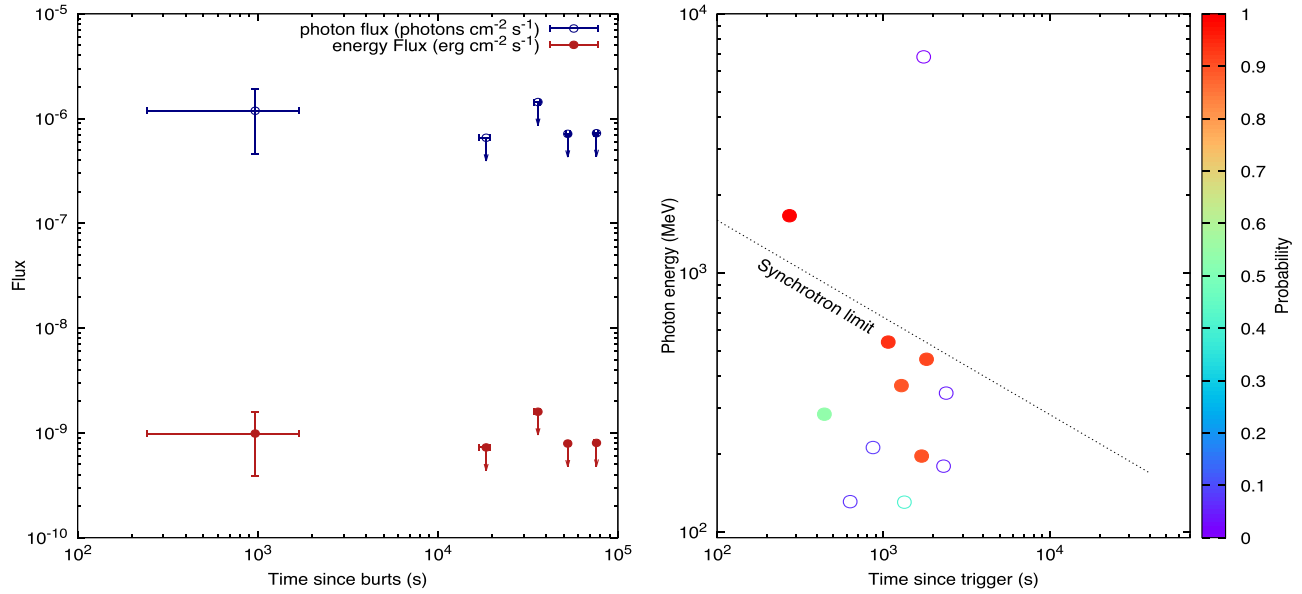

Figure 6. The left panel shows the Fermi-LAT energy flux (blue) and photon flux (red) light curves obtained between 0.1 and 100 GeV. The right panel shows all of the photons with energies >100 MeV and their respective probabilities of being associated with GRB 130702A. The dotted line corresponds to the synchrotron limit.

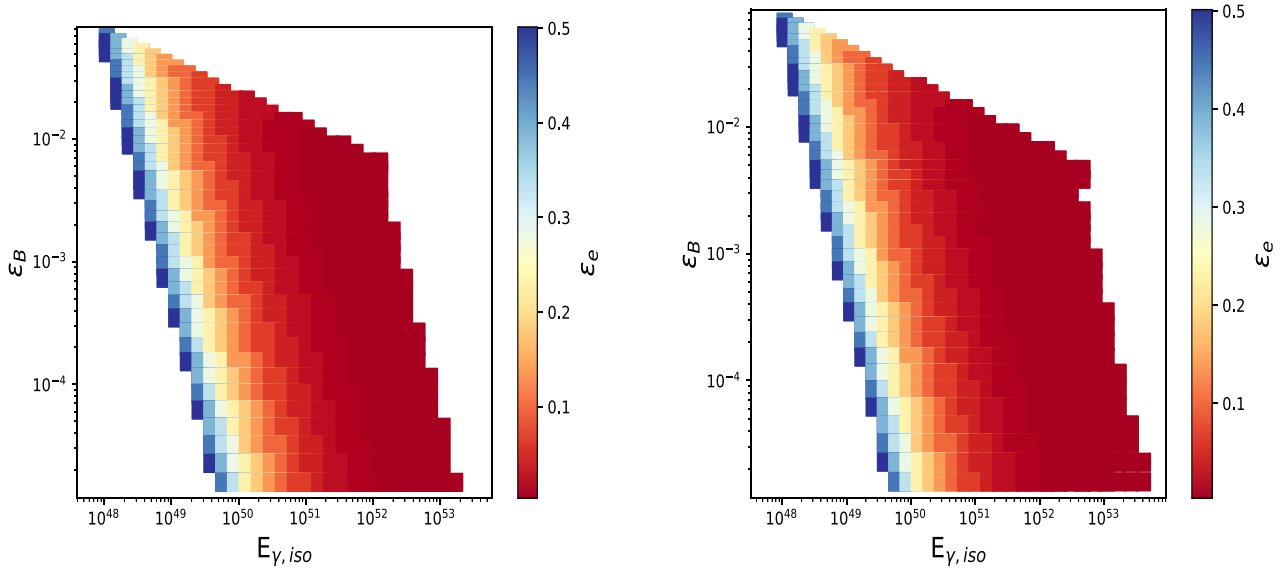

Figure 7. The panels show the 3D parameter space of the microphysical parameters and isotropic energy for which the SSC flux from FS is below (left) and above five times (right) the LAT sensitivity at 10 GeV and above the H.E.S.S. sensitivity at 80 GeV (Piron 2016). The values of $n = 1$ cm^{-3}, $p = 2.1$, and $z = 0.2$ are considered.

can detect VHE photons from ilGRBs with the condition that the gamma-ray emission is below and slightly above (five times)[22] the Fermi-LAT sensitivity. In both cases, we consider the EBL model derived by Franceschini & Rodighiero (2017) and the values of $n = 1$ cm^{-3}, $p = 2.1$, and $z = 0.2$.

5.6.2.1. Below the Fermi-LAT Sensitivity

We plot the parameter space for which VHE gamma-ray emission can be detected in H.E.S.S. telescopes but not in Fermi-LAT. The left panel in Figure 7 shows the parameter space of the microphysical parameters and isotropic-equivalent energy for which the SSC flux is below the Fermi-LAT sensitivity at 10 GeV and above the H.E.S.S. sensitivity at 80 GeV (Piron 2016). In particular, this panel shows that for $E_{\gamma,\rm iso} \approx 10^{48}$ erg, the set of parameters that satisfy the conditions are $\varepsilon_{\rm e} \gtrsim 0.3$ and $\varepsilon_{\rm B} \gtrsim 10^{-2}$, and for $E_{\gamma,\rm iso} \approx 10^{53}$ erg, the parameters become $\varepsilon_{\rm e} \lesssim 0.1$ and $\varepsilon_{\rm B} \lesssim 10^{-5}$.

5.6.2.2. Slightly above the Fermi-LAT Sensitivity

We plot the parameter space for which VHE gamma-ray emission can be detected in the H.E.S.S. telescopes and also slightly detectable in Fermi-LAT. The right panel in Figure 7 shows the parameter space of the microphysical parameters and isotropic-equivalent energy for which the SSC flux is above the H.E.S.S. sensitivity at 80 GeV (Piron 2016) and slightly above the Fermi-LAT sensitivity at 10 GeV. In particular, this panel shows that for $E_{\gamma,\rm iso} \approx 10^{48}$ erg, the set of parameters are

[22] This value approximately corresponds to the difference between the upper limits derived in GRB 190829A and the observed flux in GRB 130702A.

$\varepsilon_e \gtrsim 0.5$ and $\varepsilon_B \gtrsim 5 \times 10^{-2}$, and for $E_{\gamma,iso} \approx 5 \times 10^{53}$ erg, the parameters become $\varepsilon_e \lesssim 0.1$ and $\varepsilon_B \lesssim 10^{-5}$.

6. Summary

One of the closest bursts to Earth, GRB 190829A was followed by a large number of satellites and observatories in several wavelengths ranging from radio bands to hundreds of GeV gamma rays. Analysis of the prompt gamma-ray emission pointed to GRB 190819A as an intermediate-luminosity burst ($10^{48.5}$ erg $\lesssim L_{iso} \lesssim 10^{49.5}$ erg), and modeling the X-ray and optical light curves together with its SED indicated that the outflow expanded with an initial bulk Lorentz factor of $\Gamma \simeq 34$, which is high for an llGRB (e.g., $\Gamma \lesssim 10$) and low for an hlGRB (e.g., $\Gamma \gtrsim 100$). Thus, GRB 190829A becomes the first intermediate-luminosity burst to be detected in the VHE gamma-ray band by an IACT and, in turn, the first event that was not simultaneously observed by the Fermi-LAT instrument.

Our results indicate that no photons with energies above $\geqslant$100 MeV can be associated with GRB 190829A. We found that the emission produced by internal energy dissipation in the magnetar model can explain the plateau phase. The X-ray and optical observations are consistent with synchrotron FS emission evolving between the characteristic and cooling spectral breaks during the early/coasting phase and late afterglow in a uniform-density medium. Using the best-fit parameters found after modeling the X-ray and optical light curves of GRB 190829A, we show that the VHE emission reported by the H.E.S.S. telescopes cannot be interpreted in the synchrotron FS scenario, so an additional mechanism should be present during the FSs to explain the multi-GeV photons. We interpret the energetic photons above the synchrotron limit in the SSC FS scenario. It is worth noting that the synchrotron FS model can explain the high-energy photons detected by Fermi-LAT below the synchrotron limit. We conclude that VHE emission detected above the synchrotron limit in GRB 190829A was due to (i) the very low redshift with an intermediate luminosity, (ii) the place of VHE flux origin, (iii) the favorable set of parameters, (iv) the KN regime much above hundreds of GeV, and finally, (5) a quick location by the H.E.S.S. telescope.

To date, there is only one confirmed ilGRB SN detected with $z \lesssim 0.2$: GRB 130702A. We obtained the Fermi-LAT light curve with its upper limits around the reported position of GRB 130702A and all photons with energies larger than >100 MeV. With a probability of >90%, three high-energy photons of 1661, 540, and 464 MeV were detected during the afterglow phase at 272, 1070, and 1818 s, respectively. We showed that the synchrotron FS model could not explain the highest-energy photon. Therefore, an additional mechanism such as SSC should be present during the FSs to explain this GeV energy photon.

Considering that the synchrotron FS model is insufficient to explain the high-energy and VHE photons in the two ilGRBs, we finally computed the parameter space so that SSC flux originating in these objects could be detected by the H.E.S.S. telescopes. We showed that low-redshift bursts with intermediate luminosities are potential candidates to be detected in VHEs.

N.F. acknowledges financial support from UNAM-DGAPA-PAPIIT through grant IN106521. R.B.D. acknowledges support from the National Science Foundation under grant 1816694.

ORCID iDs

N. Fraija https://orcid.org/0000-0002-0173-6453
P. Veres https://orcid.org/0000-0002-2149-9846
P. Beniamini https://orcid.org/0000-0001-7833-1043
A. Galvan-Gamez https://orcid.org/0000-0001-5193-3693
B. D. Metzger https://orcid.org/0000-0002-4670-7509
R. L. Becerra https://orcid.org/0000-0002-0216-3415

References

Abdalla, H., Adam, R., Aharonian, F., et al. 2019, Natur, 575, 464
Abdo, A. A., Ackermann, M., Ajello, M., et al. 2009, ApJL, 706, L138
Abeysekara, A. U., Archer, A., Benbow, W., et al. 2018, ApJ, 857, 33
Acciari, V. A., Aliu, E., Arlen, T., et al. 2011, ApJ, 743, 62
Acciari, V. A., Ansoldi, S., Antonelli, L. A., Engels, A. A., et al. 2019, Natur, 575, 459
Aharonian, F., Akhperjanian, A. G., Barres de Almeida, U., et al. 2009a, A&A, 495, 505
Aharonian, F., Akhperjanian, A. G., Barres DeAlmeida, U., et al. 2009b, ApJ, 690, 1068
Ahlgren, B., Larsson, J., Nymark, T., et al. 2015, MNRAS, 454, L31
Ajello, M., Arimoto, M., Axelsson, M., et al. 2019, ApJ, 878, 52
Albert, J., Aliu, E., Anderhub, H., et al. 2007, ApJ, 667, 358
Aleksić, J., Ansoldi, S., Antonelli, L. A., et al. 2014, MNRAS, 437, 3103
Amati, L. 2006, MNRAS, 372, 233
Amati, L., Frontera, F., Tavani, M., et al. 2002, A&A, 390, 81
Arnaud, K. A. 1996, in Astronomical Data Analysis Software and Systems V, ASP Conf. Ser., 101, ed. G. H. Jacoby & J. Barnes (San Francisco, CA: ASP), 17
Ashall, C., Mazzali, P. A., Pian, E., et al. 2019, MNRAS, 487, 5824
Band, D., Matteson, J., Ford, L., et al. 1993, ApJ, 413, 281
Barniol Duran, R., & Kumar, P. 2009, MNRAS, 395, 955
Barniol Duran, R., & Kumar, P. 2011, MNRAS, 412, 522
Barniol Duran, R., Nakar, E., Piran, T., & Sari, R. 2015, MNRAS, 448, 417
Barthelmy, S. D., Cannizzo, J. K., Gehrels, N., Cusumano, G., Mangano, V., et al. 2005, ApJL, 635, L133
Bartoli, B., Bernardini, P., Bi, X. J., et al. 2017, ApJ, 842, 31
Becerra, R. L., Watson, A. M., Fraija, N., Butler, N. R., Lee, W. H., et al. 2019, ApJ, 872, 118
Beloborodov, A. M. 2003, ApJL, 585, L19
Beniamini, P., Barniol Duran, R., & Giannios, D. 2018, MNRAS, 476, 1785
Beniamini, P., Duque, R., Daigne, F., & Mochkovitch, R. 2020, MNRAS, 492, 2847
Beniamini, P., & Giannios, D. 2017, MNRAS, 468, 3202
Beniamini, P., Giannios, D., & Metzger, B. D. 2017, MNRAS, 472, 3058
Beniamini, P., & Kumar, P. 2016, MNRAS, 457, L108
Beniamini, P., & Mochkovitch, R. 2017, A&A, 605, A60
Beniamini, P., Nava, L., Duran, R. B., & Piran, T. 2015, MNRAS, 454, 1073
Beniamini, P., & Piran, T. 2014, MNRAS, 445, 3892
Bernardini, M. G., Campana, S., Ghisellini, G., et al. 2013, ApJ, 775, 67
Bhat, P. N., Briggs, M. S., Connaughton, V., et al. 2012, ApJ, 744, 141
Bloom, J. S., Kulkarni, S. R., Djorgovski, S. G., et al. 1999, Natur, 401, 453
Bolmer, J., Greiner, J., & Chen, T. W. 2019, GCN Circ., 25651, 1
Bromberg, O., Nakar, E., & Piran, T. 2011, NIMPA, 389, 81
Brun, R., & Rademakers, F. 1997, NIMPA, 389, 81
Bucciantini, N., Quataert, E., Metzger, B. D., et al. 2009, MNRAS, 396, 2038
Burgess, J. M., Bégué, D., Ryde, F., et al. 2016, ApJ, 822, 63
Campana, S., Colpi, M., Mereghetti, S., Stella, L., & Tavani, M. 1998, A&ARv, 8, 279
Campana, S., Colpi, M., Mereghetti, S., Stella, L., Tavani, M., et al. 2006, Natur, 442, 1008
Cano, Z., Bersier, D., Guidorzi, C., et al. 2011, ApJ, 740, 41
Cano, Z., de Ugarte Postigo, A., Pozanenko, A., et al. 2014, A&A, 568, A19
Cano, Z., Izzo, L., de Ugarte Postigo, A., et al. 2017, A&A, 605, A107
Chand, V., Banerjee, A., Gupta, R., et al. 2020, ApJ, 898, 42
Chevalier, R. A. 1989, ApJ, 346, 847
Chevalier, R. A., & Li, Z.-Y. 2000, ApJ, 536, 195
Chincarini, G., Moretti, A., Romano, P., et al. 2007, ApJ, 671, 1903
de Naurois, M. & H.E.S.S. Collaboration 2019, GCN Circ., 25677, 1
de Ugarte Postigo, A., Bremer, M., & Kann, D. A. 2019, GCN Circ., 25589, 1

D'Elia, V., Campana, S., D'Aì, A., et al. 2018, A&A, 619, A66
D'Elia, V., Pian, E., Melandri, A., et al. 2015, A&A, 577, A116
Derishev, E. V., Kocharovsky, V. V., & Kocharovsky, V. V. 1999, ApJ, 521, 640
Dermer, C. D., & Mitman, K. E. 2004, in ASP Conf. Ser. 312, Third Rome Workshop on Gamma-Ray Bursts in the Afterglow Era, 25552 (San Francisco, CA: ASP), 301
Dichiara, S., Bernardini, M. G., & Burrows, D. N. 2019, GCN Circ., 25552, 1
Evans, P. A., Willingale, R., Osborne, J. P., et al. 2010, A&A, 519, A102
Fan, Y. Z., & Wei, D. M. 2004, ApJL, 615, L69
Fan, Y. Z., & Wei, D. M. 2005, MNRAS, 364, L42
Fraija, N. 2014, ApJ, 787, 140
Fraija, N. 2015, ApJ, 804, 105
Fraija, N., Barniol Duran, R., Dichiara, S., & Beniamini, P. 2019a, ApJ, 883, 162
Fraija, N., De Colle, F., Veres, P., et al. 2019b, ApJ, 871, 123
Fraija, N., Dichiara, S., Pedreira, A. C. C. d. E. S., et al. 2019c, ApJ, 885, 29
Fraija, N., Laskar, T., Dichiara, S., et al. 2020, ApJ, 905, 112
Fraija, N., Lee, W., & Veres, P. 2016, ApJ, 818, 190
Fraija, N., Lee, W. H., Araya, M., et al. 2017a, ApJ, 848, 94
Fraija, N., Pedreira, A. C. C. d. E. S., & Veres, P. 2019d, ApJ, 871, 200
Fraija, N., & Veres, P. 2018, ApJ, 859, 70
Fraija, N., Veres, P., Zhang, B. B., et al. 2017b, ApJ, 848, 15
Franceschini, A., & Rodighiero, G. 2017, A&A, 603, A34
Fukugita, M., Ichikawa, T., Gunn, J. E., et al. 1996, AJ, 111, 1748
Funk, S., Hinton, J. A. & CTA Consortium 2013, APh, 43, 348
Galama, T. J., Vreeswijk, P. M., van Paradijs, J., et al. 1998, Natur, 395, 670
Gao, H., Lei, W.-H., Zou, Y.-C., Wu, X.-F., & Zhang, B. 2013, NewAR, 57, 141
Gao, H., & Zhang, B. 2015, ApJ, 801, 103
Ghirlanda, G., Nava, L., Ghisellini, G., et al. 2012, MNRAS, 420, 483
Goad, M. R., Page, K. L., Godet, O., et al. 2007, A&A, 468, 103
Golkhou, V. Z., & Butler, N. R. 2014, ApJ, 787, 90
Gould, R. J., & Schréder, G. 1966, PhRvL, 16, 252
H.E.S.S. Collaboration, Abramowski, A., Aharonian, F., et al. 1992, RSPTA, 371, 20120275
Hjorth, J., Sollerman, J., Møller, P., et al. 2003, Natur, 423, 847
Hjorth, J. 2013, RSPTA, 371, 20120275
Huang, L.-Y., Wang, X.-G., Zheng, W., et al. 2018, ApJ, 859, 163
Izzo, L., de Ugarte Postigo, A., Maeda, K., et al. 2019, Natur, 565, 324
James, F., & Roos, M. 1975, Comput. Phys. Commun., 10, 343
Kobayashi, S. 2000, ApJ, 545, 807
Krimm, H. A., Yamaoka, K., Sugita, S., et al. 2009, ApJ, 704, 1405
Kumar, P., & Barniol Duran, R. 2009, MNRAS, 400, L75
Kumar, P., & Panaitescu, A. 2000, ApJL, 541, L51
Kumar, P., & Zhang, B. 2015, PhR, 561, 1
Lai, T. L., Robbins, H., & Wei, C. Z. 1978, PNAS, 75, 3034
Lattimer, J. M., & Schutz, B. F. 2005, ApJ, 629, 979
Lazarian, A., Zhang, B., & Xu, S. 2019, ApJ, 882, 184
Lazzati, D., & Begelman, M. C. 2010, ApJ, 725, 1137
Liang, E.-W., Yi, S.-X., Zhang, J., et al. 2010, ApJ, 725, 2209
Lü, H.-J., & Zhang, B. 2014, ApJ, 785, 74
Lundman, C., Pe'er, A., & Ryde, F. 2013, MNRAS, 428, 2430
Martinez-Castellanos, I. 2019, arXiv:1908.06122
McMahon, E., Kumar, P., & Panaitescu, A. 2004, MNRAS, 354, 915
Metzger, B. D., Beniamini, P., & Giannios, D. 2018, ApJ, 857, 95
Metzger, B. D., Giannios, D., Thompson, T. A., et al. 2011, MNRAS, 413, 2031
Nakar, E., Ando, S., & Sari, R. 2009, ApJ, 703, 675
Nakar, E., & Sari, R. 2012, ApJ, 747, 88
Norris, J. P., Bonnell, J. T., Kazanas, D., et al. 2005, ApJ, 627, 324
Oates, S. R., Dichiara, S. & Swift/UVOT Team 2019, GCN Circ., 25570, 1
O'Brien, P. T., Willingale, R., Osborne, J., et al. 2006, ApJ, 647, 1213
Osborne, J. P., Page, K. L., Capalbi, M., et al. 2019, GCN Circ., 25568, 1
Parfrey, K., Spitkovsky, A., & Beloborodov, A. M. 2016, ApJ, 822, 33
Pe'er, A., Mészáros, P., & Rees, M. J. 2006, ApJ, 652, 482
Piran, T., & Nakar, E. 2010, ApJL, 718, L63
Piro, A. L., & Ott, C. D. 2011, ApJ, 736, 108
Piron, F. 2016, CRPhy, 17, 617
Piron, F., Longo, F., Axelsson, M., et al. 2019, GCN Circ., 25574, 1
Planck Collaboration, Aghanim, N, & Akrami, Y. 2018, A&A, 641, A6
Quataert, E., & Kasen, D. 2012, MNRAS, 419, L1
Roming, P. W. A., Vanden Berk, D., Pal'shin, V., et al. 2006, ApJ, 651, 985
Ryde, F., & Pe'er, A. 2009, ApJ, 702, 1211
Sari, R., & Mészáros, P. 2000, ApJL, 535, L33
Sari, R., & Piran, T. 1999a, ApJ, 520, 641
Sari, R., & Piran, T. 1999b, A&AS, 138, 537
Sari, R., Piran, T., & Narayan, R. 1998, ApJL, 497, L17
Schulze, S., Malesani, D., Cucchiara, A., et al. 2014, A&A, 566, A102
Tagliaferri, G., Goad, M., Chincarini, G., et al. 2005, Natur, 436, 985
Takahashi, K., Murase, K., Ichiki, K., Inoue, S., & Nagataki, S. 2008, ApJL, 687, L5
Tan, J. C., Matzner, C. D., & McKee, C. F. 2001, ApJ, 551, 946
Terreran, G., Fong, W., Margutti, R., et al. 2019, GCN Circ., 25664, 1
Toy, V. L., Cenko, S. B., Silverman, J. M., et al. 2016, ApJ, 818, 79
Uhm, Z. L., & Zhang, B. 2014, NatPh, 10, 351
Valeev, A. F., Castro-Tirado, A. J., Hu, Y. D., et al. 2019, GCN Circ., 25565, 1
Vedrenne, G., & Atteia, J.-L. 2009, Gamma-Ray Bursts (Berlin: Springer)
Veres, P., Zhang, B.-B., & Mészáros, P. 2012, ApJL, 761, L18
Vestrand, W. T., Wren, J. A., Wozniak, P. R., et al. 2006, Natur, 442, 172
Vurm, I., & Beloborodov, A. M. 2016, ApJ, 831, 175
Vurm, I., Beloborodov, A. M., & Poutanen, J. 2011, ApJ, 738, 77
Wang, X.-Y., He, H.-N., Li, Z., Wu, X.-F., & Dai, Z.-G. 2010, ApJ, 712, 1232
Wang, X.-Y., Liu, R.-Y., Zhang, H.-M., Xi, S.-Q., & Zhang, B. 2019, ApJ, 884, 117
Woosley, S. E. 1993, ApJ, 405, 273
Woosley, S. E., & Bloom, J. S. 2006, ARA&A, 44, 507
Woosley, S. E., & Heger, A. 2012, ApJ, 752, 32
Xiao, D., & Dai, Z.-G. 2019, ApJ, 878, 62
Yi, S.-X., Wu, X.-F., & Dai, Z.-G. 2013, ApJ, 776, 120
Zhang, B. 2019, Natur., 575, 448
Zhang, B., Fan, Y. Z., Dyks, J., et al. 2006, ApJ, 642, 354
Zhang, B., & Mészáros, P. 2001, ApJ, 559, 110
Zhang, B., & Pe'er, A. 2009, ApJL, 700, L65